Excited state dynamics in SO2. I. Bound state relaxation studied by time-resolved photoelectron-photoion coincidence spectroscopy

Author(s):
Wilkinson, Iain; Boguslavskiy, Andrey E.; Mikosch, Jochen; Bertrand, Julien B.; Wörner, Hans Jakob; Villeneuve, David M.; Spanner, Michael; Patchkovskii, Serguei; Stolow, Albert

Excited state dynamics in SO2. I. Bound state relaxation studied by time-resolved photoelectron-photoion coincidence spectroscopy

Iain Wilkinson, Andrey E. Boguslavskiy, Jochen Mikosch, Julien B. Bertrand, Hans Jakob Wörner, David M. Villeneuve, Michael Spanner, Serguei Patchkovskii, and Albert Stolow

Excited state dynamics in SO₂. I. Bound state relaxation studied by time-resolved photoelectron-photoion coincidence spectroscopy

Iain Wilkinson,[1,a)] Andrey E. Boguslavskiy,[1,2] Jochen Mikosch,[1,3,b)] Julien B. Bertrand,[1,2,c)]
Hans Jakob Wörner,[1,4] David M. Villeneuve,[1] Michael Spanner,[1] Serguei Patchkovskii,[1,d)]
and Albert Stolow[1,2,3,e)]

[1]National Research Council of Canada, 100 Sussex Drive, Ottawa, Ontario K1A OR6, Canada
[2]Department of Physics, University of Ottawa, MacDonald Hall, 150 Louis Pasteur, Ottawa, Ontario K1N 6N5, Canada
[3]Department of Physics, Queen's University, 99 University Avenue, Kingston, Ontario K7L 3N6, Canada
[4]Laboratorium für Physikalische Chemie, ETH Zürich, Vladimir-Prelog-Weg 2, 8093 Zürich, Switzerland

The excited state dynamics of isolated sulfur dioxide molecules have been investigated using the time-resolved photoelectron spectroscopy and time-resolved photoelectron-photoion coincidence techniques. Excited state wavepackets were prepared in the spectroscopically complex, electronically mixed $(\tilde{B})^1B_1/(\tilde{A})^1A_2$, Clements manifold following broadband excitation at a range of photon energies between 4.03 eV and 4.28 eV (308 nm and 290 nm, respectively). The resulting wavepacket dynamics were monitored using a multiphoton ionisation probe. The extensive literature associated with the Clements bands has been summarised and a detailed time domain description of the ultrafast relaxation pathways occurring from the optically bright $(\tilde{B})^1B_1$ diabatic state is presented. Signatures of the oscillatory motion on the $(\tilde{B})^1B_1/(\tilde{A})^1A_2$ lower adiabatic surface responsible for the Clements band structure were observed. The recorded spectra also indicate that a component of the excited state wavepacket undergoes intersystem crossing from the Clements manifold to the underlying triplet states on a sub-picosecond time scale. Photoelectron signal growth time constants have been predominantly associated with intersystem crossing to the $(\tilde{c})^3B_2$ state and were measured to vary between 750 and 150 fs over the implemented pump photon energy range. Additionally, pump beam intensity studies were performed. These experiments highlighted parallel relaxation processes that occurred at the one- and two-pump-photon levels of excitation on similar time scales, obscuring the Clements band dynamics when high pump beam intensities were implemented. Hence, the Clements band dynamics may be difficult to disentangle from higher order processes when ultrashort laser pulses and less-differential probe techniques are implemented. [http://dx.doi.org/10.1063/1.4875035]

I. INTRODUCTION

The first electronically excited singlet states of sulfur dioxide, SO₂, have been studied extensively for more than 80 years and remain spectroscopically interesting. The dynamics occurring following excitation to these states represent an opportunity to study non-adiabatic interactions and relativistic effects at the small molecule limit where a confluence between experiment and theory is attainable. Early spectroscopic studies of SO₂ provided fundamental insights into the electronic structure of polyatomic molecules, with SO₂ being one of the original examples of molecules exhibiting a Douglas effect.[1] SO₂ was also one of the first polyatomic species found to exhibit an excited state Zeeman effect.[2,3] It is now known that these effects are a manifestation of non-adiabatic interactions between the electronically excited $(\tilde{B})^1B_1$ and $(\tilde{A})^1A_2$ diabatic states[4–16] and perturbations by the underlying triplet manifold,[2,3,17–19] respectively. It is these interactions that are responsible for the complex absorption profile associated with the first excited singlet states of SO₂ shown in Fig. 1. The principle electronic determinants of these and other electronically excited states that are relevant to this work are shown in Table I.

The absorption profile associated with the lowest-lying electronically excited singlet states of SO₂ was studied by Watson and Parker[20] and later by Clements.[21] Clements reported a thorough analysis of the vibrational band structure within a normal mode framework of an isolated electronic state, labelling each band with a letter that resulted in these features becoming collectively known as the Clements bands. This analysis highlighted irregularities in the frequencies and intensities of the absorption features. The perturbations responsible for these irregularities have hampered the accurate determination of the excited state vibrational frequencies and the origin of the progression to this day. From an energy domain perspective, each Clements letter band is associated with a limited number of $^1B_1$ a_1 levels that are vibronically coupled

---

a)Iain.Wilkinson@nrc-cnrc.gc.ca
b)Present address: Max-Born-Institut für Nichtlineare Optik und Kurzzeitspektroskopie im Forschungsverbund Berlin e.V., Max-Born-Str. 2 A, 12489 Berlin, Germany.
c)Present address: Max-Planck-Institut für Quantenoptik, Hans-Kopfermann-Str. 1, D-85748 Garching, Germany.
d)Serguei.Patchkovskii@mbi-berlin.de. Present address: Max-Born-Institut für Nichtlineare Optik und Kurzzeitspektroskopie im Forschungsverbund Berlin e.V., Max-Born-Str. 2 A, 12489 Berlin, Germany.
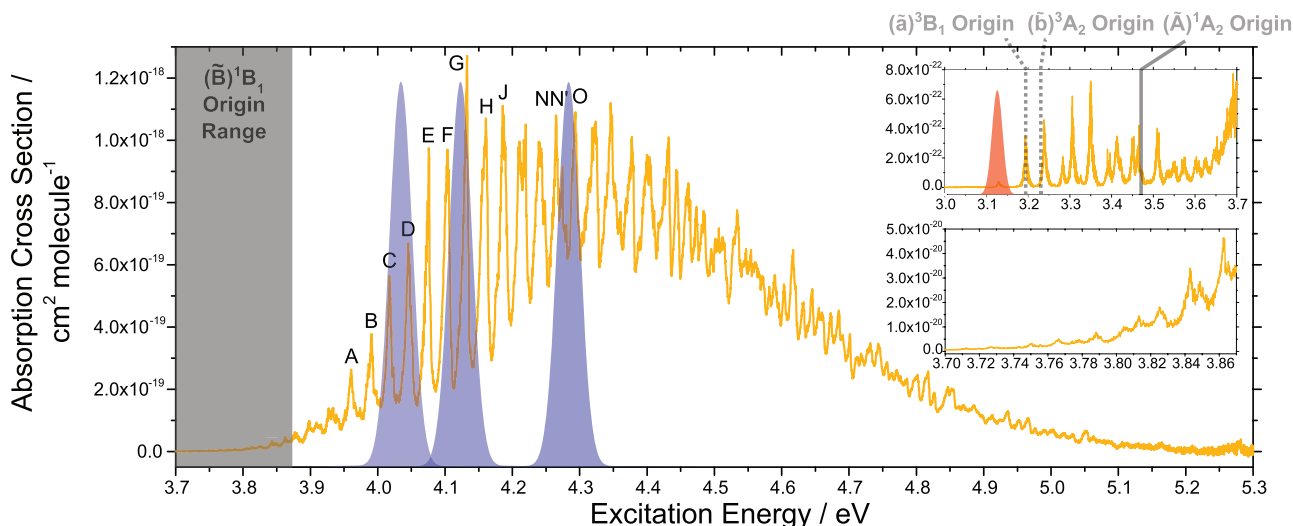e)Albert.Stolow@nrc-cnrc.gc.ca

FIG. 1. Room temperature, gas phase absorption spectrum of SO_2 recorded by Vandaele *et al.*[30] showing the profile of the Clements bands. Electronic term energies for the states associated with the profile are noted on the spectrum.[5,10,12,22,74,76,103,104] For the $(\tilde{B})^1B_1$ state, the spectroscopic origin is not well-defined. The energetic range over which the term energy has been reported is denoted on the main panel by the gray overlay. The origin shown for the $(\tilde{b})^3A_2$ state is that inferred from the work of Huang *et al.*[76] The (blue, main figure) spectral profiles of the femtosecond excitation laser pulses used in this study are overlaid at the relevant excitation energies, the (red) probe pulse spectrum is shown in the upper right inset. The principle discrete absorption bands have been labelled in accord with the notation used by Clements.[21]

to a larger number of $^1A_2$ b_2 levels via the asymmetric stretch coordinate, resulting in hybrid vibronic bands.[7,13–15,22–24] The spin-orbit interaction of these states with the triplet manifold

TABLE I. State labels, dominant electronic determinants, and experimentally determined electronic term energies, T_0, of some of the valence and Rydberg states of neutral SO_2 that are relevant to this work. Active-space orbitals used in the potential energy surface calculations of the neutral species are indicated in the $(\tilde{X})^1A_1$ state principle electronic determinant entry by the darker font. One more active virtual orbital ($2a_2$) was included in Koopmans' correlations and ionisation potential calculations. Occupation numbers given for the $(\tilde{X})^1A_1$ state correspond to the leading determinant. The characters of the remaining states and all of the other electronic states discussed in this paper are given relative to this determinant. A term energy was unavailable for the $(\tilde{d})^3A_1$ state so a vertical excitation energy from the ground electronic state equilibrium configuration (T_v) is presented.

Neutral state	Principle electronic determinant	T_0 (eV)
$(\tilde{X})^1A_1$	$(5a_1)^2(3b_2)^2(6a_1)^2$	0
	$(4b_2)^2(7a_1)^2(2b_1)^2$	
	$(5b_2)^2(1a_2)^2(8a_1)^2$	
	$(3b_1)^0(9a_1)^0(6b_2)^0$	
$(\tilde{A})^1A_2$	$(5b_2)^{-1}(3b_1)^1$	$3.50,^{74}$ $3.46^{10,12,104}$
$(\tilde{B})^1B_1$	$(8a_1)^{-1}(3b_1)^1$	$3.75–3.99^{4,5,12,22}$
$(\tilde{C})^1B_2$	$(1a_2)^{-1}(3b_1)^1$	5.278^{105}
$(\tilde{E})$	Multiple states[87,93,95]	$7.5–8.5^{87,88}$
$(2)^1A_1$	$(8a_1)^{-2}(3b_1)^2-$	
	$(2b_1)^{-1}(3b_1)^1$	
$(\tilde{G})4p_x\tilde{X}^+$	$(8a_1)^{-1}4p_x^{87,90,91}$	$9.768^{89,91}$
$(\tilde{G}')$		10.05^{89}
$(\tilde{H})4p\tilde{A}^+$	$(5b_2)^{-1}4p^{91}$	10.80^{88}
$(\tilde{a})^3B_1$	$(8a_1)^{-1}(3b_1)^1$	$3.195^{74,76,103}$
$(\tilde{b})^3A_2$	$(5b_2)^{-1}(3b_1)^1$	$\sim3.2(1)^{76}$
$(\tilde{c})^3B_2$	$(1a_2)^{-1}(3b_1)^1$	
$(\tilde{d})^3A_1$	$(2b_1)^{-1}(3b_1)^1$	$7.8(1)$ $(T_v)^{106}$
$(\tilde{g})4p_x\tilde{X}^+$	$(8a_1)^{-1}4p_x^{91}$	9.701^{91}

further complicates the absorption profile.[2,3,17–19] With additional Coriolis coupling occurring within the $(\tilde{B})^1B_1/(\tilde{A})^1A_2$ manifold[25] and possibly to the electronic ground state,[26] a labyrinthine spectroscopy ensues.

A time-domain perspective on excitation to the Clements bands and the initial dynamics in the electronically excited singlet states was presented by Köppel and co-workers.[9,27,28] A vibrational wavepacket is prepared on the optically bright $(\tilde{B})^1B_1$ diabatic surface with the Franck-Condon (FC) region spanning the conical intersection (CI) between the $(\tilde{B})^1B_1$ and $(\tilde{A})^1A_2$ diabatic states.[28,29] Here, the $(\tilde{B})^1B_1/(\tilde{A})^1A_2$ lower adiabatic surface (LAS) is predominantly excited ($\sim85\%$) with the resulting singlet state dynamics primarily occurring on this surface.[9,28,29] The majority of the upper adiabatic surface (UAS) population (corresponding to an initial $\sim15\%$) has been calculated to non-adiabatically decay to the LAS within ~15 fs with small portions of the excited state wavepacket transferring back to the UAS at later times.[9,28,29] On the LAS, the potential energy gradients along the asymmetric stretch and bending coordinates (see Fig. 2) give rise to a pseudo-Jahn-Teller instability around the CI that directs the majority of the excited state wavepacket away from regions of strong non-adiabatic coupling; preserving the LAS population. Due to the topography of the LAS, the wavepacket acquires $(\tilde{A})^1A_2$ electronic character as it bifurcates and skirts around the $(\tilde{B})^1B_1/(\tilde{A})^1A_2$ CI in both directions.

The discrete, Clements band, structure observed in the absorption spectrum[30] shows, through the inverse level spacing, that a significant portion of the excited state wavepacket undergoes a number of recursions to the FC region with a ~145 fs period. Dynamics calculations suggest that these recursions are associated with periodic orbit motions around the CI on the LAS.[9,27–29] This excited state motion involves periodic, large-amplitude bending motion, and switching of the dominant electronic character. Considering the
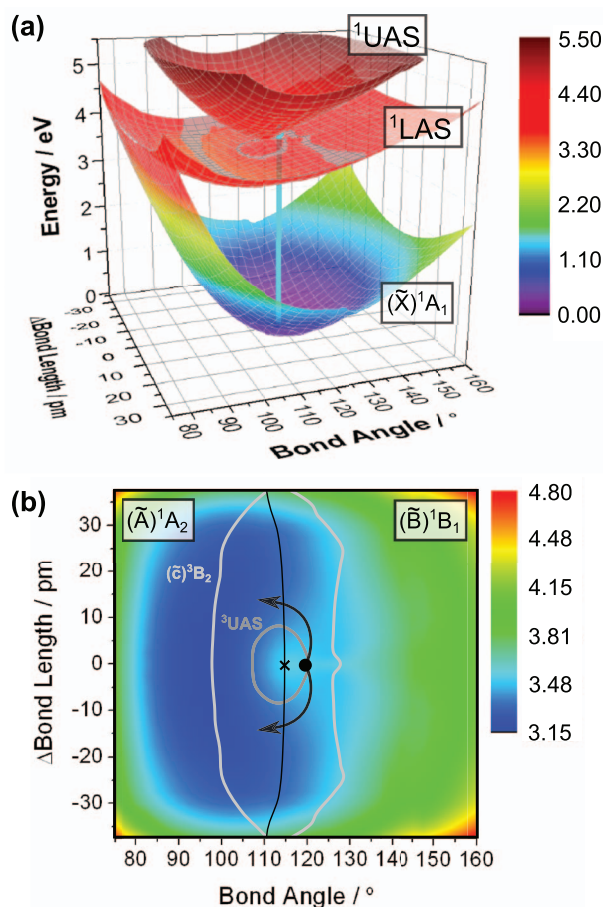
FIG. 2. Low-lying, neutral adiabatic electronic potential energy surfaces of SO$_2$. In both panels, the colour map denotes the electronic potential energy associated with different points of the nuclear coordinate space in units of eV. (a) The first three singlet adiabatic surfaces of SO$_2$ plotted along the bending angle and difference in bond length coordinates. The surfaces are the $(\tilde{X})^1A_1$ ground state, $(\tilde{B})^1B_1/(\tilde{A})^1A_2$ lower adiabatic surface (^{1}LAS) and $(\tilde{B})^1B_1/(\tilde{A})^1A_2$ upper adiabatic surface (^{1}UAS). The gray regions mark areas of proximity with the underlying triplet adiabatic states (i.e., within 50 meV). Panel (b) focuses on the $(\tilde{B})^1B_1/(\tilde{A})^1A_2$ lower adiabatic surface (LAS). The ground state equilibrium geometry and centre of the Franck-Condon (FC) window for pump photon absorption is denoted by the black dot with the position of the conical intersection indicated by the black cross. The black curve that spans the difference in bond length coordinate highlights the dividing line between dominant $(\tilde{A})^1A_2$ and $(\tilde{B})^1B_1$ electronic character on the singlet LAS. Curves highlighting the crossing coordinates with the $(\tilde{a})^3B_1/(\tilde{b})^3A_2$ upper adiabatic surface (labelled ^{3}UAS, inner curve) and the $(\tilde{c})^3B_2$ (outer curve) adiabatic surface are also shown.

quasi-continuum[31] underlying the Clements bands, aperiodic wavepacket motion is also expected to occur on the $(\tilde{B})^1B_1/(\tilde{A})^1A_2$ LAS. Through the periodic and aperiodic motions, changes in the vibrational character of the wavepacket are expected. This intramolecular vibrational energy redistribution (IVR) has been shown to occur on a sub-ten-nanosecond time scale by Bae *et al.* through time-resolved fluorescence experiments.[32] On shorter time scales, loss of population from the $(\tilde{B})^1B_1/(\tilde{A})^1A_2$ LAS is expected to occur due to intersystem crossing (ISC) to the underlying triplet manifold.[2,17,18,24,33] An experimental measurement of the time scale associated with ISC does not appear to have been reported in the literature. However, this process has been investigated using *ab initio* surface-hopping[29] and *ab initio*

wavepacket propagation calculations.[34] The former results are reported in the companion paper by Mai, Marquetand, and González that will be referred to as Paper II[29] from here onwards. The principle conclusion of Paper II[29] is that these spin-changing transitions are ultrafast in nature, in agreement with the results of the experiments reported here.

In SO$_2$, photodissociation occurs following excitation above an energy of 5.669 eV (218.7 nm).[35] In the experiments reported here, single-pump-photon absorption exclusively populates bound states. However, due to a relatively high second-photon absorption cross-section,[36,37] resonantly enhanced two-pump-photon excitation and fragmentation readily takes place following laser pumping. The two-photon excited states accessed through this process have been shown to be short-lived through time-resolved mass spectrometry (TRMS) studies.[38,39] In these TRMS experiments, sub-picosecond two-photon excited state lifetimes were extracted based on similar parent ion decay and sulfur monoxide, SO, ion signal growth time constants. With this in mind, parallel relaxation pathways are expected to occur in SO$_2$ following excitation with femtosecond laser pulses, with each relaxation route expected to produce changes in electronic and nuclear structure. Therefore, a highly differential measurement of the excited state evolution is required to gain a good understanding of the molecular dynamics associated with the first singlet absorption system.

With knowledge of the states excited and the ionic states that correlate with the populated neutral electronic configurations, the time-resolved photoelectron spectroscopy (TRPES) technique[40,41] allows the resolution of both the electronic character and vibrational energy content of evolving neutral states as a function of time. However, if many neutral states can be accessed at different levels of excitation, numerous different cation states can be produced. In such situations, it can become difficult to uniquely assign features in TRPES spectra. This problem is exacerbated when multiphoton ionisation (MPI) probes are implemented. With these MPI probes likely being resonantly enhanced, resulting in changes in electronic configuration and potentially ion state correlation, additional information is generally required to uniquely correlate dispersed electron signals with specific neutral and ionic states. By implementing the time-resolved photoelectron-photoion coincidence (TRPEPICO) method,[40] signals associated with neutral fragmentation and/or higher-lying dissociative ion states can be differentiated from non-dissociative dynamics and ionisation occurring to low-lying, stable cation states.[42]

For the above reasons, we have employed a combination of the TRPES and TRPEPICO methods to monitor the dynamics and excitation processes occurring in SO$_2$ following excitation to a number of different Clements bands between 4.03 and 4.28 eV (308 nm and 290 nm, respectively). The excited state dynamics were probed using a three- and four-probe-photon resonantly enhanced MPI scheme in order to reach the relatively high ionisation potentials of SO$_2$ (see Table II). A 3.1 eV (400 nm) probe photon energy was selected in order to minimise probe alone signals in our experiments (see the top right inset of Fig. 1). Through the correlation of the TRPES spectra with SO$_2^+$ parent ions and fragment

TABLE II. Symmetries, dominant electronic characters and experimentally determined adiabatic ionisation potentials of a number of the low-lying cation states of SO_2. The doublet ion state energetic ordering and symmetries proposed by Li *et al.*[96,107] and supported by the *ab initio* calculations reported here have been adopted. Experimentally determined T_0 values were available for the doublet states of the cation only. The term energy of the $^2B_1$ state marked as "CI Sat." corresponds to the origin of a weak set of photoelectron bands in the ground state photoelectron spectrum that have been attributed to a configuration interaction satellite ion state by Kimura *et al.*[62]

Ion state	Principle electronic determinant[87,96,107,108]	T_0 (eV)
$(\tilde{X})^2A_1$	$(8a_1)^{-1}$	12.346(3)[60,61,64,109]
$(\tilde{A})^2B_2$	$(5b_2)^{-1}$	12.988(8)[61,109,110]
$(\tilde{B})^2A_2$	$(1a_2)^{-1}$	13.338(1),[61]
		13.24(3)[84,85,109,110]
$(\tilde{C}')^2B_1$ (CI Sat.)	$(5b_2)^{-2}(3b_1)^1$	14.7(2)[62-64]
$(\tilde{C})^2B_1$	$(2b_1)^{-1}$	15.903(3)[61,64,85,109-111]
$(\tilde{D})^2A_1$	$(7a_1)^{-1}$	16.335(3)[61,109-112]

ions, we were, in general, able to separate the dynamics occurring on similar time scales at the one-pump-photon and two-pump-photon levels. Through the variation of pump photon energy, relative pump and probe laser polarisations, and pump laser intensity we have assigned the dominant, resonantly enhanced ionisation pathways occurring with the implemented probe pulses following single-pump-photon excitation to the Clements bands.

Our interpretation of the TRPEPICO spectra is consistent with the SO_2 literature, the surface-hopping calculations presented in Paper II[29] and the partial simulations of the parent molecule MPI spectra presented by Lévêque, Taïeb, and Köppel,[43] from here on referred to as Paper III.[43] In combination, these three papers (consecutively published in this issue of *The Journal of Chemical Physics*) and the previous work of Lévêque *et al.*[28,34] form a concerted experimental and theo-

retical effort to elucidate the excited state molecular dynamics occurring following single-photon excitation to the Clements bands. Schematic cross-sections of some of the adiabatic surfaces associated with the initial Clements band dynamics are shown in Fig. 2. Schematic diabatic neutral and ionic potential energy curves that are relevant to the measured photoelectron spectra reported in this paper are presented for the bond angle coordinate in Fig. 3. Illustrations of the dominant parent MPI and relaxation pathways reported here are superimposed on these curves.

II. OVERVIEW

This paper, focused on the excited state dynamics of SO_2 following excitation to the Clements bands, is organised as follows. In Sec. III, we elaborate on the methodology used in the TRPEPICO experiments and to perform the *ab initio* electronic structure calculations. In Sec. IV, we present the relevant potential energy surfaces of SO_2 and a subset of the experimental data sets. Supplementary results from the electronic calculations are presented in Subsection 1 of the Appendix. In Sec. V, our findings are discussed leading to a detailed time domain description of the ultrafast relaxation dynamics occurring following broadband excitation to the Clements bands. In Subsection V A we gauge our experimental observations and *ab initio* calculations against the exhaustive neutral state and cation manifold literature of SO_2. This is followed by Sec. V B, where an interpretation of the photoelectron bands in the $^{32}SO_2^+$ TRPEPICO spectra and low pump beam intensity $^{32}SO^+$ TRPEPICO spectra is presented (see Subsection 2 of the Appendix for a more detailed analysis). In Sec. V C we use the analysis presented in Sec. V B and Subsection 2 of the Appendix to interpret the TRPEPICO spectra and identify the dominant single-pump-photon excited state relaxation pathways. In
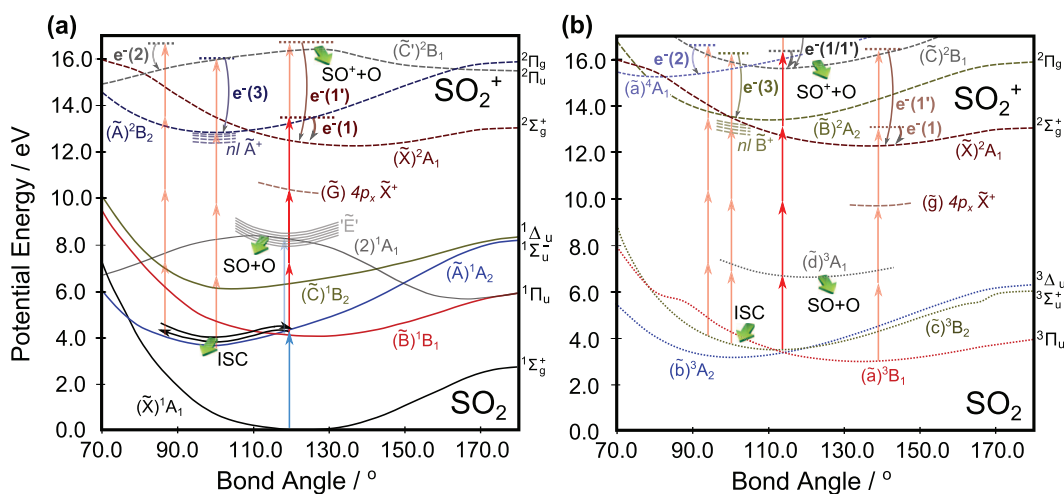
FIG. 3. MPI pathway summary showing the sources of the long-lived photoelectron bands associated with the parent ion. Panels (a) and (b) show the singlet and triplet state ionisation pathways, respectively. The schematic diabatic potential energy curves were adapted from the results of the *ab initio* calculations with the exception of the $(2)^1A_1$ state which was adapted from the works of Kamiya and Matsui[8] and Katagiri *et al.*[93] In contrast to the other potential curves shown, this surface represents the adiabatic potential leading to the first $^1\Pi_u$ state at linearity. The ionisation pathways thought to lead to SO_2^+ photoelectron bands (1), (2), (3), and (1') are denoted by the "e$^-$(1)," "e$^-$(2)," "e$^-$(3)," and "e$^-$(1')" arrows, respectively. These ionisation pathways are discussed in detail in Subsection 2 of the Appendix. A two-pump-photon excitation route to a set of (pre)dissociative singlet states ("Ẽ") that lead to neutral SO and O (and likely S and O_2) fragments is also shown in panel (a). This process is thought to be partially responsible for the appreciable SO^+ yields and the pump beam intensity dependent time constants extracted from the SO_2^+ data (see Sec. V D).

Subsection V C 1, the predominantly adiabatic, periodic motion occurring on the $(\tilde{B})^1B_1/(\tilde{A})^1A_2$ LAS is discussed. In Subsection V C 2, the spin-orbit induced ISC pathways from the $(\tilde{B})^1B_1/(\tilde{A})^1A_2$ LAS are discussed. In Subsection V D, we describe resonantly enhanced two-pump-photon excitation processes leading to dynamics that may obscure the Clements band relaxation processes when high-pump beam intensities are implemented. Those readers who are interested in the single-pump-photon initiated, Clements band dynamics alone may skip over this subsection. Finally, concluding remarks are presented in Sec. VI. In synopsis, with the recent results of Lévêque *et al.*[28, 34] and those presented in Papers II[29] and III,[43] this paper presents a unified time domain description of the relaxation processes occurring in SO_2 following excitation to the Clements bands.

III. METHODS

Ultrashort pump pulses were generated from a titanium-sapphire based oscillator-regenerative amplifier-cryogenic amplifier laser chain (Coherent Inc.). The laser chain ran with a central fundamental photon energy of 1.559 eV or 1.545 eV (795.5 or 802.5 nm) for the experiments reported here, delivering 9 mJ pulse^{-1} with 35 fs pulse durations (full-width at half-maximum, FWHM) at a 1 kHz repetition rate. The majority of the laser output (7 mJ pulse^{-1}) was directed to an optical parametric amplifier (OPA, Light Conversion Ltd. HE-TOPAS) with a portion of the signal output being twice frequency doubled in separate $BaBO_4$ (BBO) crystals (300 μm and 150 μm thick, respectively). Propagation to the experimental chamber produced slightly positively chirped pump pulses of $\sim$50 fs duration (FWHM) at the laser-molecular beam interaction region. These pulse duration estimates were based on autocorrelations of the OPA signal output, the dispersion characteristics of the transmissive materials in the pump beam line and cross-correlation measurements of the pump and probe pulses in the TRPEPICO spectrometer (discussed below). Pump photon energies between 4.03 and 4.28 eV and bandwidths of $\sim$50 meV (FWHM, measured using a USB4000 Ocean Optics Inc. spectrometer) were implemented in separate experiments.

Probe pulses were generated by frequency doubling a portion of the fundamental beam in a thin BBO crystal (300 μm) resulting in probe photon energies of either 3.12 eV or 3.09 eV (397.5 nm or 401.2 nm, depending on the fundamental frequency of the laser chain). The probe pulse durations were estimated to be $\sim$60 fs (FWHM) at the laser-molecular beam interaction region based on autocorrelation measurements of the fundamental beam, the dispersion characteristics of the transmissive optics in the probe beam line, and cross-correlation measurements of the pump and probe pulse in the TRPEPICO spectrometer. A corresponding 30 meV bandwidth (FWHM) was measured for the probe pulses. The probe pulses were collinearly recombined with the pump pulses through the back of a pump beam line dielectric mirror aligned close to zero degrees.

The pump and probe pulses were directed to the experimental chamber, where the beams were mildly focused using a protected aluminium spherical mirror (1 m radius-of-curvature). Pump pulse energies of 0.1–3 μJ were implemented for all experiments, corresponding to cycle averaged, spatial peak pump pulse intensities between 0.1 and 1.5 $\times 10^{12}$ W cm^{-2} at the molecular beam (a cycle averaged, spatial peak definition of pulse intensity is used throughout this paper). Probe pulse energies of 5–7 μJ were implemented resulting in intensities of $\sim$4 $\times 10^{12}$ W cm^{-2}. Cross-correlations for the experiments were determined *in situ* to be between 75 and 95 fs through the non-resonant, [1+3′] and [1+4′] ionisation of H_2O (where the photon ordering is arbitrary). We use "unprimed" and "primed" numbers in square brackets to indicate the number of pump and probe photons absorbed, respectively, in the different processes discussed in this paper.

The PEPICO spectrometer used to carry out these experiments has been described in Ref. 42. A 1% mixture of SO_2 (BOC Canada Ltd., 3.8N purity) in He (Praxair Canada Inc., 5N purity) was continuously expanded through a 50 μm pinhole into a source chamber held at a pressure of $\sim$3 $\times 10^{-6}$ Torr (molecular beam on). The molecular beam was skimmed to a diameter of $\sim$1 mm and orthogonally intersected by collinear, co-propagating pump and probe laser beams $\sim$600 mm from the pinhole in a separate detection chamber held at a base pressure of $\sim$5 $\times 10^{-8}$ Torr (molecular beam on). Photoelectrons were extracted from the laser-molecular beam interaction region by a novel large bore permanent magnet, magnetic bottle spectrometer.[44] A pulsed Wiley-McLaren time-of-flight (TOF) mass-spectrometer[45] was used to extract the photoions in the opposite direction for coincident detection. Photoelectron and photoion TOFs were separately detected using a pair of triple stack microchannel plates backed by collection anodes. The resulting signals were amplified, constant fraction discriminated and recorded using different channels of a multichannel scaler card (FAST Comtec GmbH P788). The photoelectron and photoion detection efficiencies were both $\sim$40%. Each total TRPES spectrum and associated time-resolved mass spectrum was generated by scanning the pump-probe delay over a range of -400 to $+100\,000$ fs with variable step sizes. Scans were performed with high-temporal resolution (20–50 fs steps) between -400 and $+2000$ fs only. Pump-probe signals were recorded for 7500 laser shots, whereas weak, time-independent probe alone signals were recorded for 750 laser shots at each pump-probe delay. The photoelectron and photoion TOF spectra were stored for each laser shot. The pump-probe delay range was swept through 30–85 times depending on signal strength and signal-to-noise levels. Linearly polarised laser pulses were employed, measurements were performed with the relative pump-probe laser polarisations set parallel, perpendicular, and at magic angle (54.7°). Polarisation states were set using a waveplate in the probe laser beam line and analysed after recombination using a Glan-Taylor polariser (Melles Griot 03 PTA 001).

The photoelectron and mass spectra measured with each laser shot were post-processed by calculating the covariance[46–48] of the signals associated with each electron TOF bin and the total photoion signals associated with specific ion TOF bin ranges (i.e., mass peaks). For each pump-probe delay, the photoelectron-photoion covariance spectra were constructed by summing the covariant photoelectron

signals associated with each ion TOF (mass) bin range and electron TOF bin. Iterating this process over the pump-probe delay range produced the TRPEPICO spectra associated with the different ions. In the data presented here, covariant probe-alone signals have been subtracted from all pump-probe TR-PEPICO spectra (all spectra were normalised to the total number of laser shots to facilitate this procedure). Negligible signals were observed from the pump beam alone. The TRPEPICO TOF spectra were photoelectron kinetic energy calibrated through four and five photon MPI of neat xenon using the probe laser beam alone. These measurements, along with the H_2O cross-correlation measurements, also facilitated the mass calibration of the TRPEPICO spectrometer.

The calibrated TRPEPICO spectra were analysed using a 2D global least-squares method to fit the temporal profiles associated with a range of photoelectron kinetic energies, $S(E,t)$, simultaneously.[49] These fits incorporated the FWHM of the experimental cross-correlation, c, and time-zero, t_0, determined from separate Gaussian fits to the temporal profiles of H_2O^+ ion signals and/or bands in the covariant photoelectron spectra. These cross-correlation functions and the minimum number of exponential decay components to non-trivially fit the experimental data provided a basis for the 2D global fits.[49] For positive delays, the cross-correlation profile was convoluted with the sum of the exponential decay components and the amplitudes of the cross-correlation and exponential decay components were allowed to vary as a function of photoelectron kinetic energy. A didactic example of the function applied for a parallel biexponential fit to a TR-PEPICO spectrum is shown in Eq. (1):

$$S(E,t) = A_0(E)\exp\left(-\frac{(t-t_0)^2}{2\sigma^2}\right) \otimes \begin{cases} \left(A_1(E)\exp\left(-\frac{t}{\tau_1}\right) + A_2(E)\exp\left(-\frac{t}{\tau_2}\right)\right) & \text{if } t \geq t_0 \\ 0 & \text{if } t < t_0 \end{cases}, \quad (1)$$

where $\sigma = \frac{c}{2\sqrt{2\ln 2}}$, A_0 denotes the amplitude of the cross-correlation function, $A_x(E)$ denote the photoelectron kinetic energy dependent fit amplitudes associated with temporal component x and τ_x is the exponential decay constant associated with decay component x.

The convoluted temporal components associated with the fits were optimised by adjusting the amplitudes of the fit components and the exponential decay constants to minimise the value of χ^2 for the experimental data and the fit using a mixture of Levenberg-Marquardt, stochastic, and exhaustive search routines. From the optimised fits, we extract the time constants (encompassing the fitted energy range) and the photoelectron kinetic energy dependence of the fit amplitudes associated with each temporal fit component. The 1D kinetic energy profiles of the fit amplitudes represent the photoelectron spectrum of all features with common temporal behaviour and are termed decay associated spectra (DAS).[49,50] Examples of the DAS extracted from fits to some of the data sets reported here are shown in panels (b)–(d) (high pump intensity data) and (f)–(h) (low pump intensity data) of Fig. 7. Some of the time constants extracted using the global fitting procedure are summarised in Tables III and columns two and three in Tables IV and V. We note that the time constants extracted from such global fitting procedures often reveal the average temporal behaviour associated with the fitted spectral region. Due to coupling between temporal components with similar time constants in the fitting procedure, these global fitting methods are generally unable to extract multiple time constants occurring within the same decade.

In certain cases, where individual photoelectron bands were observed with small amplitudes (resulting in these bands having little effect on the global χ^2 hypersurface), 1D fits were performed on the temporal profiles of kinetic energy integrated photoelectron bands in order to examine their time dependence independently. These fits also allowed time constants to be extracted from different bands that have similar but not equivalent temporal behaviours. The 1D fits took on a similar form to those of the 2D global fitting analysis. However, the fit component amplitudes, A_x, and time constants, τ_x, were here associated with a single temporal profile only. The results of such fits to data sets recorded with relatively low pump beam intensities and parallel and perpendicular relative laser polarisations are summarised in Tables IV and V, respectively.

We note that in both the 2D and 1D fits, positive amplitudes are signatures of the decay of the photoelectron feature at that kinetic energy, whereas negative amplitudes highlight resolvable signal growths and sequential processes. The uncertainties associated with the fits were determined by iteratively and individually varying each time constant, fixing that time constant and allowing the other time constants and all amplitudes to vary in order to minimise χ^2. The error bounds (confidence intervals) reported here are the range of each time constant over which the value of χ^2 is within 1.05 times its minimum value. These values represent both the relative fit uncertainty and the variability of the time constants over the fitted photoelectron kinetic energy range.

In our theoretical analysis, the low-lying singlet and triplet full-dimensional potential energy surfaces of SO_2 were calculated using the GAMESS-US[51] software package. Calculations of the neutral potential energy surfaces used a modified aug-cc-pVTZ basis set,[52,53] recontracted for the Douglas-Kroll scalar relativistic Hamiltonian (cc-pVTZ-DK).[54] Basis functions with $L = 3$ (f-type) were removed from the basis set. At each geometry, the 12-electron 9-orbital complete-active-space (CAS) wavefunction was optimised for a weighed average of low-lying electronic states. All states (both singlets and triplets) within 1.4 eV of the first excited state were

TABLE III. Summary of the time constants extracted from 2D global fits to the $^{32}SO_2^+$ TRPEPICO data recorded with pump photon energies of 4.12 eV and high ($\sim 1.0 \times 10^{12}$ W cm^{-2}) and low ($\sim 2.5 \times 10^{11}$ W cm^{-2}) pump beam intensities and the associated Fourier transformed spectra. Where they are reported, the τ_1 time constants are predominantly associated with exponential growth. The reduced τ_1 time constants extracted from the high pump beam intensity data are discussed in Sec. V D.

Energetic region	Relative laser polarisation	High pump intensity			Low pump intensity		
		τ_1 (fs)	τ_2 (fs)	$\tau_{osc.}$ (fs)	τ_1 (fs)	τ_2 (fs)	$\tau_{osc.}$ (fs)
[1+3′] & [1+4′] (Region A & B)	Parallel	∞	N/A	155^{+35}_{-25}	∞	N/A	160^{+30}_{-25}
	Magic angle	∞	N/A	155^{+35}_{-20}	∞	N/A	170^{+35}_{-30}
	Perpendicular	55^{+35}_{-30}	∞	155^{+40}_{-25}	200^{+80}_{-65}	∞	170^{+50}_{-30}
[1+3′] (Region A)	Parallel	∞	N/A	155^{+35}_{-25}	∞	N/A	160^{+30}_{-25}
	Magic angle	∞	N/A	155^{+35}_{-20}	∞	N/A	170^{+35}_{-30}
	Perpendicular	40^{+20}_{-15}	∞	155^{+40}_{-25}	200^{+80}_{-65}	∞	170^{+50}_{-30}
[1+4′] (Region B)	Parallel	∞	N/A	N/A	370^{+265}_{-140}	∞	N/A
	Magic angle	∞	N/A	N/A	330^{+315}_{-145}	∞	N/A
	Perpendicular	155^{+160}_{-75}	∞	N/A	230^{+210}_{-105}	∞	N/A

TABLE IV. Summary of the SO_2^+ TRPEPICO time constants extracted from 2D global fits to the [1+3′] (Region A) and [1+4′] (Region B) photoelectron kinetic energy windows, the Fourier transformed spectra, and 1D fits to the kinetic energy integrated long-lived photoelectron band temporal profiles. The time constants were extracted from the data recorded with low pump intensities ($\sim 2.5 \times 10^{11}$ W cm^{-2}) and parallel relative laser polarisations. Despite the reduction in the implemented pump beam intensity, some of the bands still displayed complex temporal profiles. These signals generally require four exponential fit components to describe their temporal evolution. However, due to the similarities of three of the time constants associated with such a fit, it is not possible to meaningfully fit the complex temporal profiles. In these situations, the three or more unknown time constants are replaced with a "Cplx." entry in the table. The time constants shown here are the results of parallel biexponential fits where one of the time constants was fixed at a large value (1×10^{11} fs, denoted in the table as $\tau = \infty$). The other exponential time constants and their associated uncertainties are shown for the different pump photon energies and energetic fit ranges in the table. Due to the low intensity of the signals in the [1+4′] region of the 4.28 eV data sets, it was not possible to produce a meaningful fit and time constants for this region. For this reason, this datum has been replaced with an *. Time constants extracted from high-pump beam intensity ($\sim 2.5 \times 10^{11}$ W cm^{-2}) data were notably shorter or more complex kinetics with respect to the low pump intensity results were observed (see Table III and Sec. V D).

$\hbar\omega_{pump}$ (eV)	Region A global fit τ_1 (fs)	Region B global fit τ_1 (fs)	$\tau_{osc.}$ (fs)	$\tau_{band(1)}$ (fs)	$\tau_{band(2)}$ (fs)	$\tau_{band(3)}$ (fs)	$\tau_{band(1')}$ (fs)
4.03	Cplx.	510^{+345}_{-175}	145^{+25}_{-20}	Cplx.	Cplx.	Cplx.	Cplx.
4.12	∞	370^{+265}_{-140}	155^{+35}_{-25}	∞	290^{+95}_{-75}	395^{+130}_{-90}	∞
4.28	∞	*	N/A	∞	355^{+155}_{-105}	Cplx.	∞

TABLE V. As Table IV but for the perpendicular relative laser polarisation data. The band profiles associated with 4.12 eV pump photon excitation are presented on the right-hand side of Fig. 7(e). The low pump beam intensity data sets that were recorded with perpendicular relative laser polarisations were well described by biexponential functions where one of the exponential time constants was fixed at a large value (1×10^{11} fs, denoted in the table as $\tau = \infty$) to yield a cross-correlation limited step function. The other exponential time constants are shown in the table for the different pump photon energies and energetic fit ranges.

$\hbar\omega_{pump}$ (eV)	Region A global fit τ_1 (fs)	Region B global fit τ_1 (fs)	$\tau_{osc.}$ (fs)	$\tau_{band(1)}$ (fs)	$\tau_{band(2)}$ (fs)	$\tau_{band(3)}$ (fs)	$\tau_{band(1')}$ (fs)
4.03	420^{+135}_{-90}	535^{+330}_{-195}	145^{+25}_{-20}	415^{+120}_{-80}	490^{+130}_{-95}	540^{+180}_{-120}	400^{+185}_{-115}
4.12	200^{+85}_{-65}	230^{+210}_{-105}	170^{+50}_{-30}	205^{+70}_{-60}	220^{+50}_{-40}	240^{+105}_{-75}	210^{+135}_{-80}
4.28	305^{+95}_{-70}	*	N/A	315^{+75}_{-65}	390^{+165}_{-105}	410^{+365}_{-170}	295^{+220}_{-125}

included with equal weights. The weight was decreased linearly, reaching zero at 2.8 eV above the first excited state. Dynamical correlation was treated using a multi-state MC-QDPT2 approach.[55,56] Scalar relativistic effects were included using a Douglas-Kroll-Hess transformation through the second order.[57] Spin-orbit effects were treated using a SO-MCQDPT2 approach.[58] Intruder-state avoidance[55,56,58] was used in all perturbative corrections.

For the calculations of the cation states, ionisation potentials, and ionisation Dyson orbitals, an unmodified aug-cc-pVQZ basis set was used, together with CAS(12,10) (neutral species) or CAS(11,10) (cations) wavefunctions. C_{2v} symmetry restricted equilibrium nuclear geometry state energies, T_e, were calculated for a number of the low-lying cation states with the cation nuclear geometries optimised at the CASSCF level. Additionally, relaxed bending mode potential energy curves were calculated for the low-lying doublet and quartet cation states. In these calculations, the symmetric stretch coordinate was optimised to its minimum energy configuration at each bond angle and the calculations were restricted to C_{2v} symmetry. Unless otherwise mentioned, all electronic states within 4.5 eV of the neutral/cation ground state were included with equal weights in the state average, regardless of the spin quantum number. Dynamical correlations were treated with MCQDPT2 corrections. Relativistic effects, both scalar and spin-orbit, were neglected for the ion state calculations.

IV. RESULTS

Results from the *ab initio* electronic structure calculations are shown in Fig. 2. In panel (a) the first three adiabatic singlet potential energy surfaces of SO_2 are plotted in a reduced coordinate space of bond angle and the difference in the bond lengths. The potential energy plotted here corresponds to the minimum with respect to the remaining coordinate (sum of the bond lengths). Upon the $(\tilde{B})^1B_1/(\tilde{A})^1A_2$ LAS associated with the CI, two gray regions are superimposed. The inner area denotes the region in coordinate space where the $(\tilde{a})^3B_1/(\tilde{b})^3A_2$ UAS (not shown) lies within 50 meV of the $(\tilde{B})^1B_1/(\tilde{A})^1A_2$ LAS. The outer "grayed" out region corresponds to the subset of the coordinate space where the $(\tilde{c})^3B_2$ surface (not shown) lies within 50 meV of the $(\tilde{B})^1B_1/(\tilde{A})^1A_2$ LAS. These regions represent areas of the coordinate space from where ISC to the triplet manifold is most likely.[59] The $(\tilde{B})^1B_1/(\tilde{A})^1A_2$ LAS is shown in more detail in panel (b). The black line spanning the difference in bond length coordinate separates regions of dominant $^1A_2$ and $^1B_1$ electronic character. The centre of the FC window (black dot), CI position (highlighting degeneracy with the corresponding UAS, black cross), $(\tilde{a})^3B_1/(\tilde{b})^3A_2$ UAS (^{3}UAS) crossing curve (inner gray curve) and the $(\tilde{c})^3B_2$ crossing curve (outer gray curve) are overlaid on the singlet LAS. Schematic excited state difference in bond length/bending mode trajectories are shown by the black arrows. Calculated neutral and ion state equilibrium energies and geometries as well as bending mode potential energy curves associated with the low-lying cation states are presented in Subsection 1 of the Appendix.

TRPEPICO spectra were recorded using the MPI probe following excitation at three different photon energies.
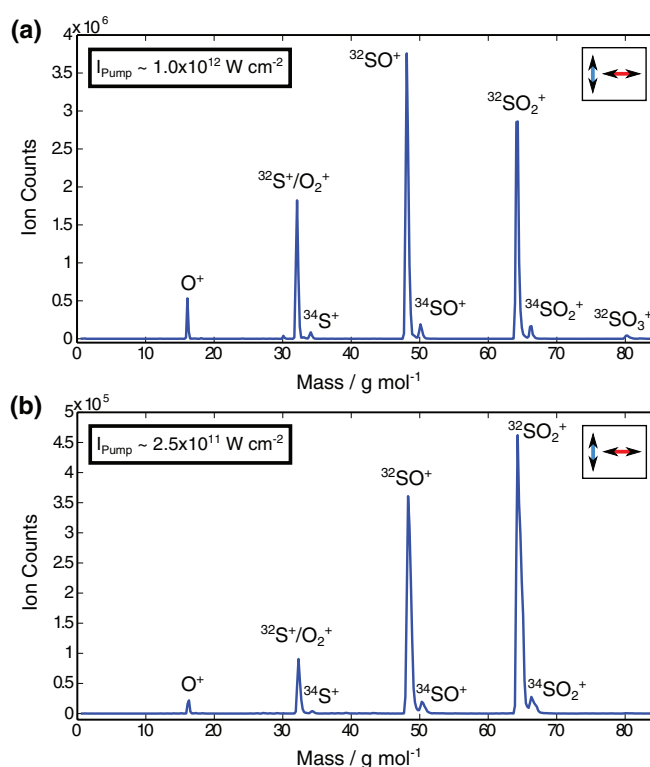

FIG. 4. Time-integrated (-0.4 to 2.0 ps) mass spectra recorded with perpendicular relative laser polarisation vectors, a pump photon energy of 4.12 eV, and a pump laser intensity of $\sim 1.0 \times 10^{12}$ W cm^{-2} (panel (a)) and $\sim 2.5 \times 10^{11}$ W cm^{-2} (panel (b)). The total ion counts per mass bin are plotted along the y-axes with the mass-to-charge ratio, m/z, plotted along the x-axes.

Additionally, the experiments were performed with three different relative laser polarisation geometries and at a variety of pump beam intensities. From each of these experiments we extracted the TRPEPICO spectra associated with the $^{32}SO_2^+$ principle isotope (95% abundant) parent ion and the associated dominant $^{32}SO^+$ and $^{32}S^+/O_2^+$ fragments. Example time-integrated (-0.4 to 2.0 ps) mass spectra are shown for the 4.12 eV pump photon energy (301 nm) and perpendicular relative laser polarisation case at two different pump beam intensities in Fig. 4. Under the conditions employed in this study, the $^{32}SO^+$ ion yield varied between 0.5 and 1.5 times that of the parent ion depending on the pump intensity, relative pump-probe polarisation vectors and the pump-photon energy. The $^{32}S^+/O_2^+$ yield was found to vary similarly, was always less than half that of the $^{32}SO^+$ fragments and had a similar TRPEPICO spectrum to the $^{32}SO^+$ fragments. This suggests that the majority of the fragments are ^{32}S born through $^{32}SO_2^+$ and/or $^{32}SO^+$ ion states. As the neutral state dynamics are imprinted in the SO_2^+ and SO^+ TRPEPICO spectra, the $^{32}S^+$ TRPEPICO spectra (or those of any of the other ionised species not mentioned above) will not be discussed further here. As the dominant photoelectron features associated with these principle ions considerably overlap in energy and display similar kinetics, separation of their photoelectron spectra through coincident ion detection significantly enhances our ability to understand the associated molecular dynamics.

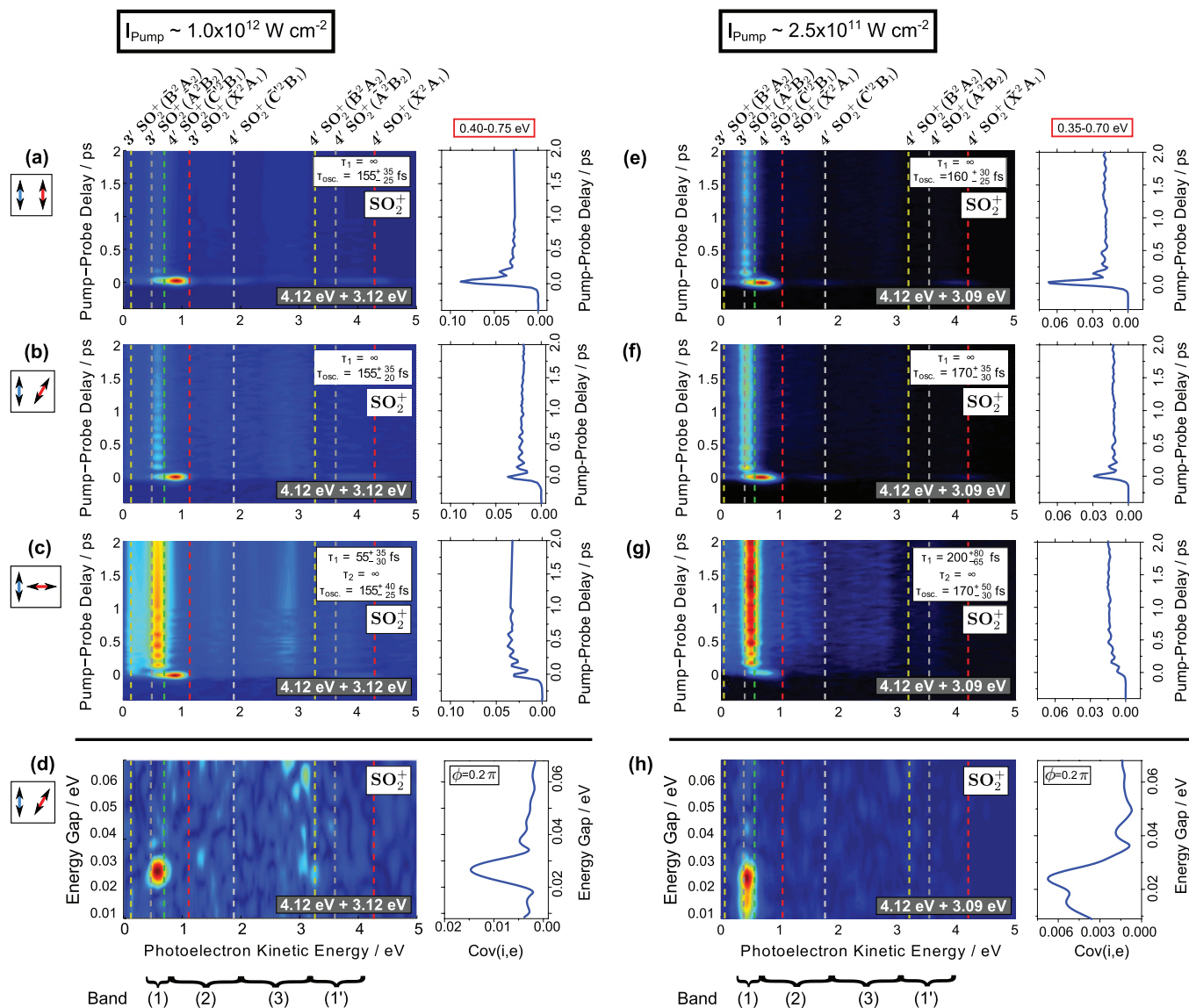In Fig. 5 we show the TRPEPICO spectra that correlate with the $^{32}SO_2^+$ parent ion for parallel, magic angle, and

FIG. 5. $^{32}SO_2^+$ TRPEPICO spectra recorded following 4.12 eV excitation and 3.1 eV multiphoton ionisation. Panels (a)–(c) show TRPEPICO spectra for experiments performed with higher pump intensities and parallel, magic angle, and perpendicular pump-probe laser polarisations, respectively. Similar data are shown in panels (e)–(g) for lower pump beam intensity experiments. Maximum photoelectron kinetic energy thresholds for [1+3′] and [1+4′] ionisation processes leading to specific ion states are denoted on the spectra by the dashed vertical lines. Intense features were observed when the pump and probe lasers were temporally overlapped, the most intense of which has an energetic cut-off equivalent to the [1+3′] threshold ionisation energy. These features are predominantly attributed to non-resonant ionisation of SO_2 at the peaks of the applied pump and probe laser fields. Similar features were observed in all of the SO_2^+ TRPEPICO spectra. The time constants (τ_1, τ_2) associated with resonant excitation in SO_2 were extracted from global fits to the [1+3′] and [1+4′] kinetic energy regions (0.0–4.3 eV) and are denoted on the associated spectra. The kinetic energy integrated temporal profiles of the principle oscillatory band, band (1), are shown to the right of each spectrum. In panels (d) and (h) we show the Fourier transformed TRPEPICO spectra for the magic angle relative polarisation geometry and the two pump intensity regimes. Associated band (1) energy gap profiles and the initial oscillatory phase shifts, ϕ, are shown to the right of each spectrum (see text for details).

perpendicular relative pump-probe laser polarisation combinations following excitation at 4.12 eV. Results are presented for two pump intensity regimes; panels (a)–(c) correspond to TRPEPICO spectra recorded with a $\sim 1.0 \times 10^{12}$ W cm^{-2} pump beam intensity, whereas panels (e)–(g) are associated with a $\sim 2.5 \times 10^{11}$ W cm^{-2} pump beam intensity. Away from the temporal overlap of the pump and probe laser fields, a sharp and long-lived, damped oscillatory electron band is observed that has a lifetime in excess of 100 ps. A number of higher energy, less intense, similarly long-lived photoelectron bands are also present. Here the red dashed lines highlight the adiabatic energetic threshold for electrons produced via

[3′] and [4′] ionisation processes to the ground $(\tilde{X})^2A_1$ state of the cation $((8a_1)^{-1}$, $T_0 = 12.346$ eV (100.42 nm)[60]). The dashed dark gray and yellow lines show similar thresholds associated with production of $^{32}SO_2^+$ in the $(\tilde{A})^2B_2$ $((5b_2)^{-1}$, $T_0 = 12.988$ eV (95.461 nm)[61]) and $(\tilde{B})^2A_2$ $((1a_2)^{-1}$, $T_0 = 13.338$ eV (92.956 nm)[61]) electronically excited ion states, respectively. Additional thresholds for [4′] ionisation to the $(\tilde{C}')^2B_1$ $((5b_2)^{-2}(3b_1)^1$, $T_0 = 14.7(2)$ eV (84.3(1.2) nm)[62–64]) and $(\tilde{C})^2B_1$ $((2b_1)^{-1}$, $T_0 = 15.903$ eV (77.963 nm)[61]) states are shown in light gray and green, respectively. We note that all of the energetic thresholds discussed in this paper do not account for the pump and probe pulse

bandwidths. Hence, photoelectron bands may stretch slightly beyond the thresholds indicated on the figures.

The time constants denoted on the ^{32}SO$_2^+$ TRPEPICO spectra in Fig. 5 were extracted using the least squares based global fitting procedure over the energy range associated with the [3'] and [4'] ionisation region (for 4.12 eV pump photons, 0–4.3 eV). The time constants were found to be pump beam intensity dependent, although the photoelectron band energetics appear to be relatively unaffected over the employed pump beam intensity range. In order to produce unique fits, the oscillatory periods were not extracted using the least squares method but were determined separately. The oscillatory components are highlighted on the right-hand side of each spectrum, where the temporal profiles of the kinetic energy integrated (~0.35–0.75 eV), dominant oscillatory photoelectron bands are plotted. In Fig. 5(d) we show a Fourier transformed SO$_2^+$ TRPEPICO spectrum associated with the higher pump intensity early pump-probe delay data recorded with magic angle relative laser polarisations. This contour plot highlights the dominant oscillatory component shown in panel (b). A similar, albeit lower signal-to-noise, contour plot associated with Fig. 5(f) is shown for the lower pump intensity data in Fig. 5(h). Using Fourier transformed TRPEPICO spectra like those shown in panels (d) and (h), early pump-probe delay oscillatory time scales and the variance of these periods have been extracted from the dominant features of the frequency profiles. These oscillation time constants, $\tau_{osc.}$, were determined through Gaussian fits to the frequency profiles and are denoted on the spectra. Oscillatory time constants were similarly extracted from the majority of the SO$_2^+$ data sets. The average oscillatory phase shifts, ϕ, associated with the data shown in Figs. 5(b) and 5(f) were also extracted through fits to the kinetic energy integrated temporal profiles. Example phase shifts of 0.2π are shown in the insets of the kinetic energy integrated frequency profiles to the right of Figs. 5(d) and 5(h). The associated phase shift fits took the form S$_{Band(1)}$(t) $\propto \cos(\omega t + \phi)$, where ω denotes the angular frequency of the oscillation. The value of ω was fixed at the mean value extracted from the frequency profiles shown in Figs. 5(d) and 5(h), to facilitate the fits.

In Fig. 6 we show the ^{32}SO$_2^+$ TRPEPICO spectra recorded with pump photon energies of 4.03, 4.12, and 4.28 eV; panels (a)–(c), respectively. The data shown in Fig. 6 were recorded with pump beam intensities of ~1.0 × 10^{12} W cm^{-2} and parallel relative laser polarisations. Similar thresholds to those presented in Fig. 5 are shown for each pump photon energy. The temporal profiles of the dominant photoelectron band (0.40–0.75 eV) are shown on the right of each spectrum. For these parallel relative laser polarisation data sets, monoexponential global fit functions were found to be appropriate where the exponential time constants were fixed at large values (1 × 10^{11} fs, labelled $\tau = \infty$ on the figure) to yield cross-correlation limited step functions. We noted that single oscillatory time scales could not be extracted from the data associated with higher pump photon energy excitation ($\hbar\omega_{pump}$ = 4.28 eV). At these photon energies, more complex temporal behaviour is expected due to the initial wavepacket preparation spanning multiple optically bright vibrational states with disparate energetic spacings and in-
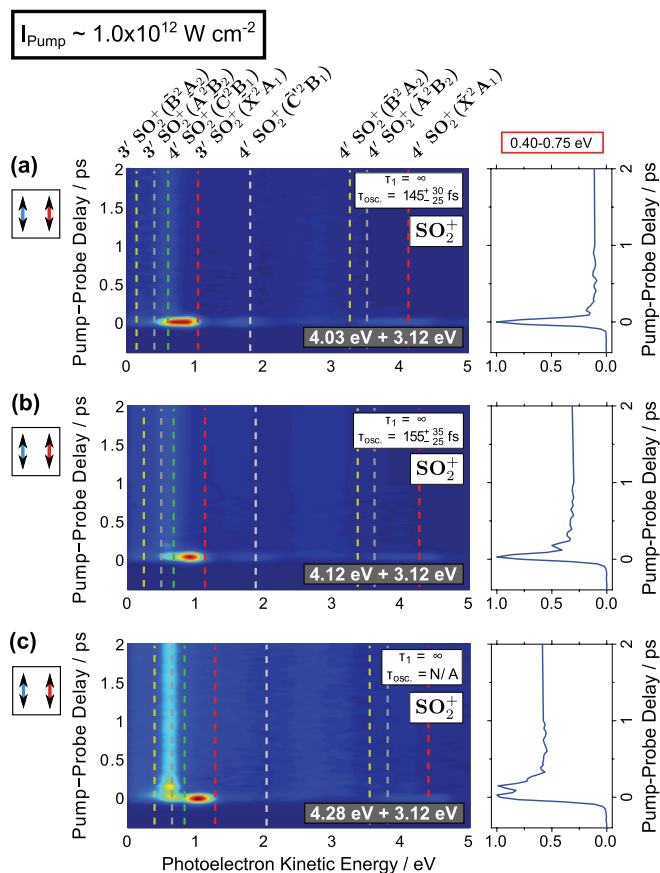

FIG. 6. TRPEPICO spectra correlated with ^{32}SO$_2^+$ following excitation between 4.03 and 4.28 eV and multiphoton ionisation at 3.12 eV. The data sets were recorded with parallel laser polarisation vectors and a pump beam intensity of ~1.0 × 10^{12} W cm^{-2}. Similar adiabatic ionisation thresholds as those superimposed on Fig. 5 have been overlaid on the spectra. The time constants extracted from global fits to the kinetic energy regions associated with both [1+3'] and [1+4'] ionisation (0–4.3 eV, regions A and B) and the Fourier transformed spectra are also shown in the top right panels on each TRPEPICO spectrum. The traces on the right-hand side of the spectra show the kinetic energy integrated (0.40–0.75 eV) temporal profiles of the principle photoelectron band (band (1)).

creasingly complex vibrational mode coupling. Hence, initial oscillatory time constants are not reported for these data sets.

In Fig. 7(a) we show the mixed time scale (−0.4 to 2.0 ps linear, 2.0–100.0 ps logarithmic) TRPEPICO spectra correlated with ^{32}SO$_2^+$ and recorded with a pump photon energy of 4.12 eV, perpendicular relative laser polarisations and a pump beam intensity of ~1.0 × 10^{12} W cm^{-2}. The temporal profiles of the principle photoelectron bands are shown to the right of the spectrum. In panels (b)–(d), the DAS extracted from the global fitting procedure performed on two energetic windows of the data shown in panel (a) are presented along with their temporal fit components. Region A spans 0–1.2 eV and is predominantly associated with [1+3'] ionisation. The associated fit results are shown by the blue curves. Region B is associated with the energetic window between 1.2 and 4.3 eV and predominantly [1+4'] ionisation. These fit results are denoted by the purple profiles. Panel (b) of Fig. 7 shows the DAS for the temporal overlap of the pump and probe laser fields whereas panels (c$_A$), (c$_B$), and (d) show similar data for the [1+3'] growth time constant, [1+4'] growth time constant and step
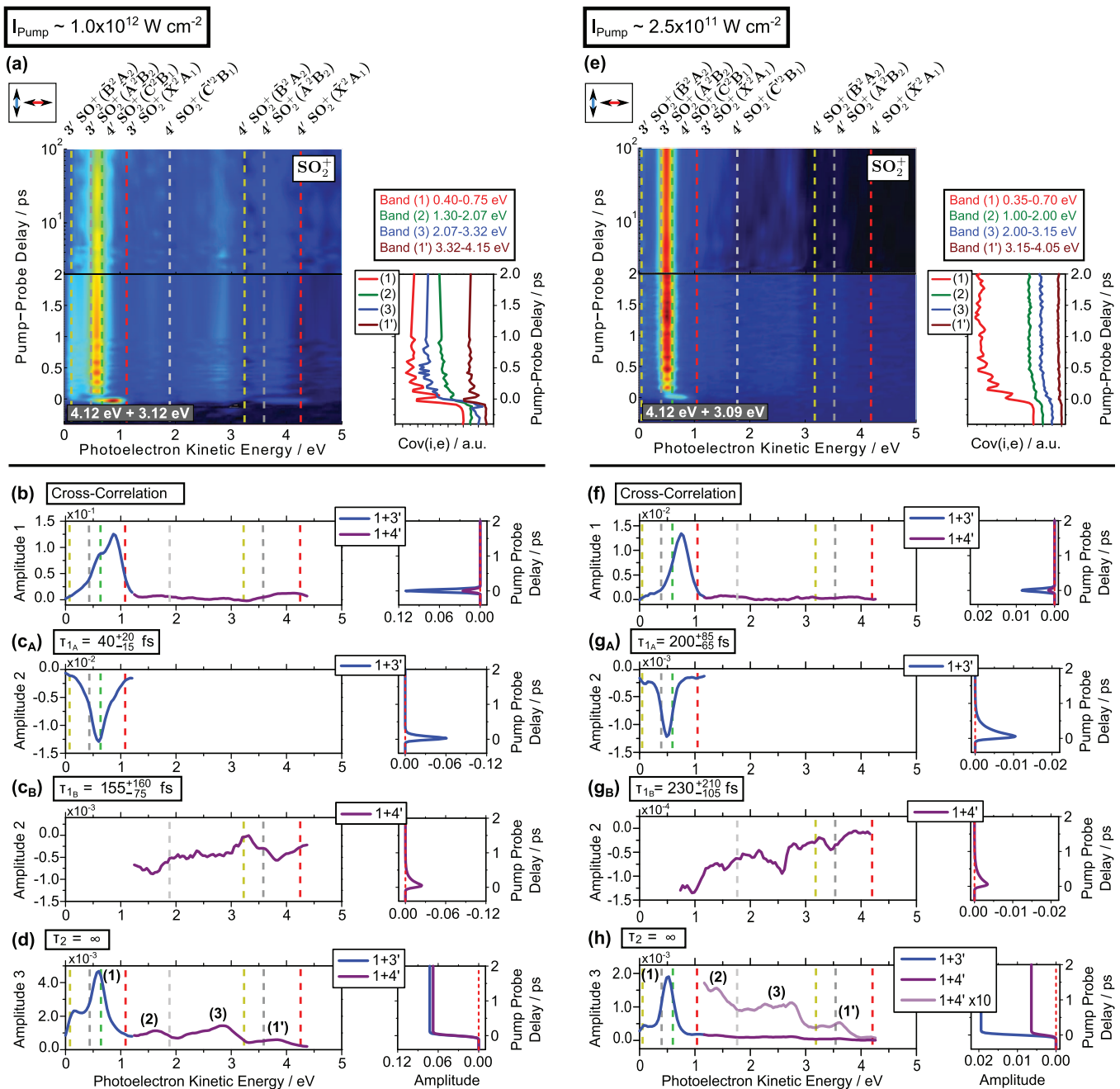
FIG. 7. Panels (a) and (e) show the mixed time scale (−0.4 to 2.0 ps linear, 2–100 ps logarithmic) TRPEPICO spectra of $^{32}SO_2^+$ recorded with a pump photon energy of 4.12 eV and perpendicular relative laser polarisations. Panel (a) corresponds to data produced with a ∼1.0 × 10^{12} W cm^{-2} pump beam intensity while panel (e) shows the data associated with a ∼2.5 × 10^{11} W cm^{-2} pump beam intensity. For the higher pump intensity data, the temporal profiles of the four main photoelectron bands are shown on the right of panel (a). The energetic profiles of the associated long-lived photoelectron bands are labelled in panel (d). These features are the SO_2^+ photoelectron bands (1), (2), (3), and (1′) referred to in the main body of the text. DAS extracted from parallel biexponential fits to the high pump intensity TRPEPICO spectrum over the energetic regions primarily attributed to [1+3′] (region A) and [1+4′] (region B) ionisation are shown in panels (b), (c_A), (c_B), and (d). The fits associated with the data spanning region A, 0.0–1.2 eV, are shown in blue whereas those associated with region B, 1.2–4.3 eV, are shown in purple. Panels (b), (c_A), (c_B), and (d) show the DAS corresponding to the pump-probe temporal overlap, 40_{-15}^{+20} fs growth component extracted from region A only, 155_{-75}^{+160} fs growth component extracted from region B only and the long-lived components (step functions, $\tau = \infty$), respectively. The temporal profiles of the four main photoelectron bands recorded with low pump intensities are shown on the right of panel (e). Similar DAS to those presented for the high pump intensity data are shown for the low pump intensity data in panels (f), (g_A), (g_B), and (h). Note the increases in the exponential growth time constants associated with panels (g_A) and (g_B) (200_{-65}^{+85} fs and 230_{-105}^{+210} fs, respectively) with respect to panels (c_A) and (c_B). The disparity of the time constants is discussed in the main body of the text (see Sec. V D).

functions, respectively. Data recorded with a pump beam intensity of 2.5 × 10^{11} W cm^{-2} is shown in panel (e). The DAS produced from global fits to this data set are shown in panels (f), (g_A), (g_B), and (h). These panels correspond to the

DAS for temporal overlap of the pump and probe laser fields, the [1+3′] growth time constant, [1+4′] growth time constant and step functions, respectively. Similar thresholds as shown in Figs. 5 and 6 are overlaid on the TRPEPICO spectra and
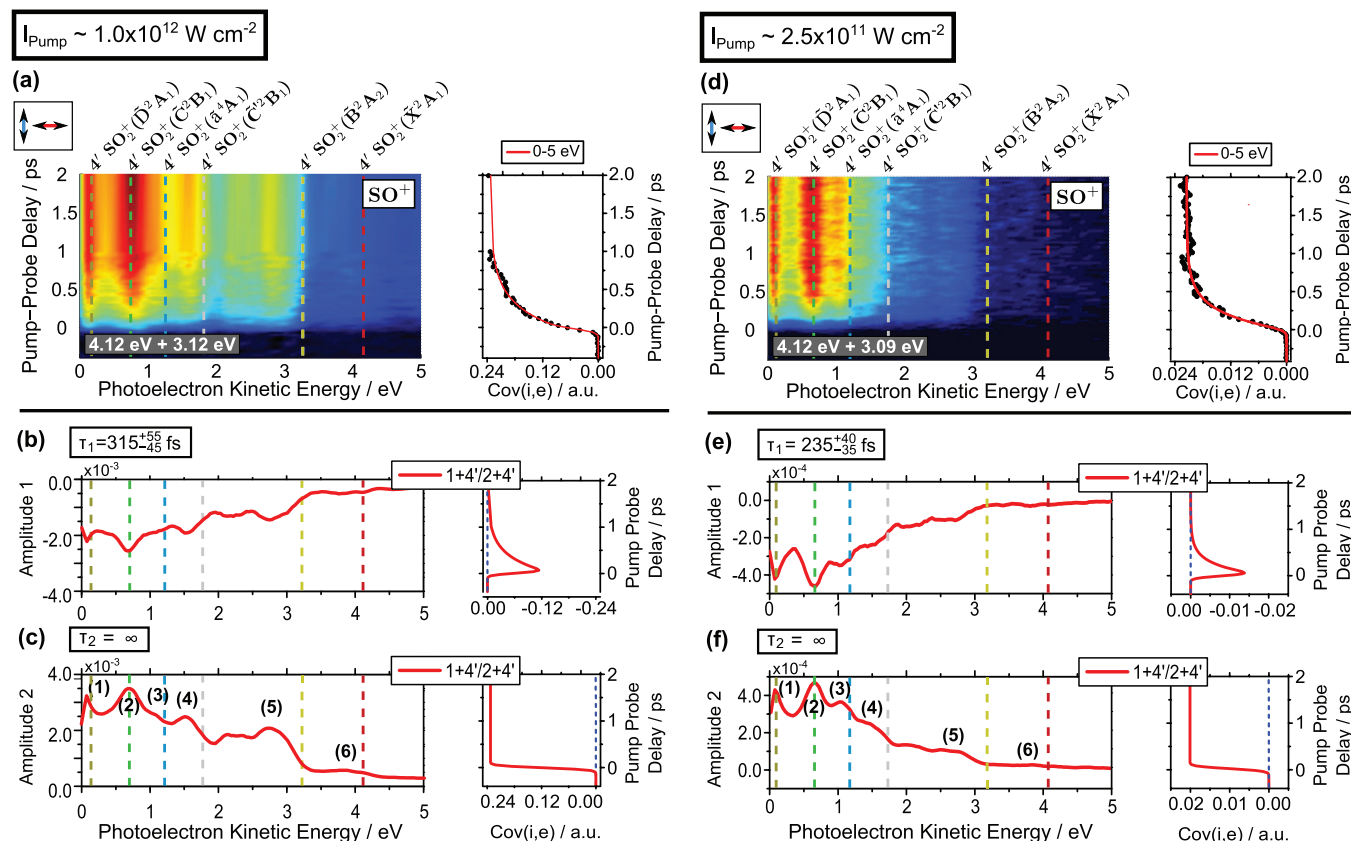
FIG. 8. $^{32}SO^+$ TRPEPICO spectra recorded with 4.12 eV pump photons and perpendicular laser polarisations. Data recorded with relatively high (I_{pump} $\sim 1.0 \times 10^{12}$ W cm^{-2}) and low ($I_{pump} \sim 2.5 \times 10^{11}$ W cm^{-2}) pump-beam intensities are shown in panels (a) and (d), respectively. Panels (b) and (c) show the DAS extracted from a parallel biexponential global fit to the high pump beam intensity data shown in panel (a). Panels (b) and (c) correspond to a 315^{+55}_{-45} fs growth component and the late-time SO^+ TRPEPICO spectrum (cross-correlation limited step function component, $\tau = \infty$). Similar DAS and features were extracted from the low pump beam intensity data shown in panel (d). These DAS are shown in panels (e) (associated with the 235^{+40}_{-35} fs growth component) and (f) (associated with the cross-correlation limited step function). Similar energetic thresholds as those overlaid on Figs. 5–7 are superimposed on the SO^+ TRPEPICO spectra and DAS. Additional energetic thresholds are shown for ionisation leading to the $(\tilde{D})^2A_1$ and $(\tilde{a})^4A_1$ states of the cation, where the latter threshold is associated with the value obtained from the electronic structure calculations. Discrete features in the late-time SO^+ TRPEPICO spectra shown in panels (c) and (f) are labelled photoelectron bands (1), (2), (3), (4), (5), and (6). The contrast of some of these features is lost when higher pump-beam intensities are implemented. Additionally, the time constants associated with the appearance of the SO^+ ions and the associated photoelectrons are noted to change with pump beam intensity (see Sec. V D and Table VII).

DAS. The growth time constants associated with the high and low pump beam intensity data were found to be markedly different.

In Figs. 8(a) and 8(d) we show the $^{32}SO^+$ TRPEPICO spectra recorded with perpendicular relative laser polarisations and relatively high ($\sim 1.0 \times 10^{12}$ W cm^{-2}) and low ($\sim 2.5 \times 10^{11}$ W cm^{-2}) pump beam intensities, respectively. The DAS extracted from the high pump beam intensity data are presented in panels (b) and (c). Similar DAS extracted from the low pump beam intensity data are presented in panels (e) and (f). Similar thresholds to those shown in Fig. 7 are overlaid on the SO^+ TRPEPICO spectra, with these thresholds highlighting the maximum kinetic energy of electrons produced with parent ions that subsequently fragmented to SO^+. Additional thresholds are shown for [1+4′] ionisation to the $(\tilde{D})^2A_1$ ($7a_1^{-1}$, $T_0 = 16.335$ eV (75.901 nm)[61]) and $(\tilde{a})^4A_1$ ($5b_2^{-1}1a_2^{-1}3b_1^1$, $T_e = 15.3(3)$ eV (81.0(1.7) nm), see Table IX) states of the cation to aid in the interpretation of the SO^+ TRPEPICO spectra. These thresholds are denoted by the dark yellow and light blue lines, respectively.

V. DISCUSSION

A. Single-pump-photon wavepacket dynamics and ionisation

1. Clements band excitation and relaxation pathways

In the experiments presented above, a number of B_1-like vibronic states encompassed by the excitation bandwidth of the pump pulses were excited following single-pump-photon absorption. At excitation energies between 4.03 and 4.28 eV, the pump pulses span two or more Clements bands, preparing different degrees of symmetric stretch and bending mode excitation in the initially excited vibrational states.[5,6,13,14,22] Specifically, the Clements C and D, F, and G and N, N′, and O bands were excited with the 4.03 eV, 4.12 eV, and 4.28 eV pump photons, respectively. The electronic and vibrational nature of the excited state evolved in time during and following the excitation process. At the single-pump-photon level of excitation for all of the pump photon energies implemented here, the internal energy is well below the first dissociation limit of SO_2. However, due to the intense nature of the pump excitation fields and the expected high cross-section for

second photon absorption,[36,37] a second pump photon may be absorbed leading to neutral fragmentation.[37–39,65,66] Signatures of further excitation by the pump field to (pre)dissociative states were observed in a number of the high pump intensity SO_2^+ data sets; particularly where parallel relative laser polarisations were implemented. The SO^+ fragments and their covariant photoelectrons produced in these experiments are thought to be partially associated with two-pump-photon absorption to short-lived, predissociative states.[38,39] It is this process that also appears to be responsible for the pump beam intensity dependent time constants reported here (see Sec. V D).

Using the gas phase absorption spectrum of SO_2 over our pump pulse bandwidths,[30] we can assess the relative contributions of the discrete and quasi-continuous spectral structure following broadband excitation at different pump photon energies. These ratios are directly related to the contributions of the periodic and aperiodic excited state wavepacket components in our time-resolved experiments. On this basis, after excitation at 4.03 and 4.12 eV, 45%–55% of the excited state wavepacket launched on the $(\tilde{B})^1B_1/(\tilde{A})^1A_2$ LAS should periodically recur to the pump pulse FC region. With a 4.28 eV excitation energy, ~20% of the excited state wavepacket is expected to periodically recur. The time scale of this recursion will be concomitant with the separation of the Clements bands (generally ~29 meV corresponding to a ~145 fs recursion time) with the damping time of this oscillatory component related to the spectral width of the excited Clements bands (6–10 meV corresponding to 400–700 fs). On short time scales, the aperiodic portion of the wavepacket is expected to evolve through a number of possible relaxation processes; diabatic or adiabatic motion followed by passage to anharmonic regions of the $(\tilde{B})^1B_1/(\tilde{A})^1A_2$ LAS and/or ISC to the triplet manifold.

Considering the Clements band literature, signatures of the majority of the accessible states at the single-pump-photon level are expected to persist over the pump-probe delay range considered here. A microsecond lifetime is expected for the optically bright $^1B_1$ levels accessed after single-photon excitation.[15,17,18,22,23,32,67–72] On longer time scales, electric dipole forbidden fluorescence has been observed to occur from the $(\tilde{A})^1A_2$ well[10,12,15,32,71] (bond angles close to 100°) via an intensity borrowing mechanism. Hence, the singlet manifold is known to be long-lived.

The triplet manifold is accessed through spin-orbit coupling, most likely at regions of coordinate space with low singlet-triplet energy gaps (see Fig. 2). Signatures of the spin-orbit interaction responsible for these processes have been observed in the energy domain throughout the Clements manifold[2,17,18,24,33] with the coupling found to persist below the origin of the $(\tilde{B})^1B_1$ diabat.[24] Experimental determinations of the time scales associated with such ISC processes have not, to our knowledge, been reported previously.

Dispersed phosphorescence measurements[15,32,71] highlight coupling, albeit said to be collisionally induced, between the Clements bands and the non-adiabatically perturbed $(\tilde{a})^3B_1$ state.[73–76] This state has been shown to have a lifetime in excess of 8 ms[10,77] and is expected to survive well beyond the pump-probe delays implemented in these experiments. The $(\tilde{a})^3B_1$ and $(\tilde{b})^3A_2$ states are known to be vibronically coupled through the asymmetric stretch coordinate[74,76] with the two states sharing similar topographies to their singlet counterparts. Hence, similar lifetimes are expected for the $(\tilde{b})^3A_2$ and $(\tilde{a})^3B_1$ states in isolated molecule experiments.

To our knowledge, no lifetime data have been reported for the $(\tilde{c})^3B_2$ state. With the weak absorption features associated with the $(\tilde{c})^3B_2$ state likely underlying the singlet absorption features (see Table I and Fig. 3), the lifetime of this state would be difficult to extract through frequency-resolved experiments. Symmetry arguments disqualify vibronic interactions between the $(\tilde{c})^3B_2$ state and the other triplet states in C_{2v} or C_s symmetry. However, population transfer to/from the $(\tilde{c})^3B_2$ state could occur through spin-orbit coupling with the $(\tilde{B})^1B_1/(\tilde{A})^1A_2$ LAS, the $(\tilde{X})^1A_1$ ground state and potentially the lower-lying $(\tilde{a})^3B_1$ and $(\tilde{b})^3A_2$ states. As the $(\tilde{c})^3B_2/(\tilde{X})^1A_1$ intersection seam occurs at reduced bond angles and at significantly higher energies than those of the pump photons implemented in these experiments, this interaction is from here on neglected. In contrast, based on the accessibility of regions of triplet-triplet intersection and the magnitude of the spin-orbit coupling matrix elements extracted from the electronic structure calculations (~7 meV corresponding to minimum triplet-triplet transfer time constants of the order of 300 fs), ultrafast transitions from the $(\tilde{c})^3B_2$ state to the $(\tilde{a})^3B_1/(\tilde{b})^3A_2$ manifold may need to be considered. With this in mind, any population of the $(\tilde{c})^3B_2$ state through ISC from the $(\tilde{B})^1B_1/(\tilde{A})^1A_2$ manifold may be transient. However, without detailed knowledge of the wavepacket dynamics in the triplet manifold, the expected lifetime of the $(\tilde{c})^3B_2$ state cannot be inferred.

2. Ionisation channels

Here and in Secs. V B and V C, we consider and correlate the dominant electronic determinants of the accessible neutral states following single-pump-photon excitation and those of any intermediate neutral and cationic states that could be populated through absorption of one or more probe photons. The principle electronic determinants of some of the relevant neutral and cationic states of SO_2 are shown in Tables I and II. Experimental term energies for the neutral and doublet ion states are also shown in these tables. To our knowledge, experimental term energies have not been reported for the quartet states of the cation. However, calculated neutral and ion state equilibrium geometries and state energies, including those of the low-lying quartet cationic states, are presented in Subsection 1 of the Appendix along with symmetric stretch relaxed, bending mode potential energy curves of the low-lying cationic states.

We couch the following in a framework where resonant ionisation pathways dominate and single-electron transitions between resonant states are most likely. For all of the diabatic electronic states considered here, the electronic wavefunctions are dominated by a single electronic determinant. Hence, a molecular orbital view of the neutral-neutral transitions and a Koopmans' picture[41] of the ionisation processes from the final neutral and correlated cation states will ad-

equately approximate the electronic correlations associated with the probe processes discussed in this subsection and the rest of the paper. With this in mind, we propose the following ionisation pathways by which the excited state wavepacket could be projected onto different states of the ionisation continuum.

Single-photon ionisation or non-resonant MPI from the optically bright $(\tilde{B})^1B_1$ $((8a_1)^{-1}(3b_1)^1$ dominant electronic character), or optically dark $(\tilde{A})^1A_2$ $((5b_2)^{-1}(3b_1)^1)$ states would be expected to occur to the $(\tilde{X})^2A_1$ $((8a_1)^{-1})$ and $(\tilde{A})^2B_2$ $((5b_2)^{-1})$ cation states, respectively. We note that the ionisation processes taking place with our MPI probe may have been resonantly enhanced by states other than Rydberg levels correlated with either of these ion states. In this situation, the Koopmans' correlation for ionisation would be associated with the accessed intermediate state, potentially changing the correlated cation state.

The $^2B_1$ $((5b_2)^{-2}(3b_1)^1)$ electronically excited state of the cation, here referred to as $(\tilde{C}')^2B_1$, could also be directly accessed via the $(\tilde{A})^1A_2$ state following pump photon absorption and nuclear motion. Weak signatures of the $(\tilde{C}')^2B_1$ state have previously been detected, despite low FC factors and the formally forbidden nature of the electronic transition, in vacuum ultraviolet ground state photoelectron spectra.[62–64, 78] The ion state potential energy curve calculations reported here highlight non-adiabatic interactions between the $(\tilde{C}')^2B_1$ and $(\tilde{C})^2B_1$ $((2b_1)^{-1})$ states (see Subsection 1 of the Appendix where curve crossings occurring close to $100°$ and $140°$ can be seen in the top panel of Fig. 14). With this in mind, the ground neutral state, single photon ionisation transitions to the $(\tilde{C}')^2B_1$ state can be attributed to an intensity borrowing mechanism. The transition to the optically dark $(\tilde{C}')^2B_1$ state gains oscillator strength through the non-adiabatic interaction with the optically bright $(\tilde{C})^2B_1$ $((2b_1)^{-1})$ state. It is this interaction that has allowed a $(\tilde{C}')^2B_1$ term energy of 14.7(2) eV to be extracted in energy-resolved experiments.[62–64] Following electronic excitation and relaxation on the $(\tilde{B})^1B_1/(\tilde{A})^1A_2$ LAS, a direct ionisation process to the $(\tilde{C}')^2B_1$ state is formally allowed with the FC factors notably improving due to the more similar equilibrium bond angle and bond lengths of the $(\tilde{A})^1A_2$ and $(\tilde{C}')^2B_1$ states with respect to the $(\tilde{X})^1A_1$ and $(\tilde{C}')^2B_1$ states (see Tables VIII and IX).

At excitation energies above 15.963 eV (below 77.669 nm),[35, 79, 80] ion state fragmentation can occur to produce $SO^+(X^2\Pi_\Omega)$ and $O(^3P_J)$ products. It is known that following excitation to the $(\tilde{C})^2B_1$ $((2b_1)^{-1})$, $(\tilde{D})^2A_1$ $((7a_1)^{-1})$ or higher-lying states of the cation at the ground state equilibrium geometry of the neutral molecule, less than 20% of the parent ions survive.[81–83] When such high-lying ion states are accessed at energies above the dissociative ionisation limit, the resulting parent ions are not expected to be stable on our ion collection time scale.[81–83] Hence, photoelectrons associated with accessing the $(\tilde{C})^2B_1$ state (with >60 meV of internal energy) or higher-lying states would be expected to at least partially correlate with SO^+ fragment ions, diminishing the signal contribution to the SO_2^+ TRPEPICO spectra. In our experiments, at least one extra probe photon would have been required to reach these higher-lying ion states with respect to the $\tilde{X}$, $\tilde{A}$, and $\tilde{B}$ ion states. Therefore, following

ionisation from the singlet manifold, a predominant sensitivity to these lower-lying doublet states is expected in the SO_2^+ TRPEPICO spectra. Due to the possibility of fluorescent relaxation and/or dissociation following ionisation, signatures of the higher-lying ion states may be expected in both the SO_2^+ and SO^+ TRPEPICO spectra. Further contributions may be made to the SO^+ TRPEPICO spectra if the stable low-lying ion states of SO_2, formed through MPI, were to absorb more probe photons. Such transitions would form unstable ion states that are likely to fragment, correlating the photoelectrons produced through MPI with the fragment ions. Partial visible and UV absorption spectra of the three lowest-lying, doublet ion states of SO_2 have previously been recorded in energy domain experiments.[84–86] Notably, the $(\tilde{B})^2A_2$ state was observed to absorb at 3.1 eV, leading to the dissociative $(\tilde{C})^2B_1$ state via a *y*-polarised transition.

If triplet states were significantly populated following broadband excitation to the Clements bands, we would expect the accessible states – $(\tilde{a})^3B_1$ $((8a_1)^1(3b_1)^{-1})$, $(\tilde{b})^3A_2$ $((5b_2)^{-1}(3b_1)^1)$, and $(\tilde{c})^3B_2$ $((1a_2)^{-1}(3b_1)^1)$ – to directly ionise to the $\tilde{X}$, $\tilde{A}$, and $\tilde{B}$ doublet ion states, respectively. Direct ionisation to the $(\tilde{C}')^2B_1$ ion state could also potentially occur from the $(\tilde{b})^3A_2$ state at reduced bond angles. Furthermore, from any triplet states accessed, a number of quartet ion states could be produced following MPI. Tables I and IX indicate that the three lowest-lying quartet states correlate with more than one of the accessible triplet states, potentially complicating the assignment of triplet ionisation pathways. Like the higher-lying doublet ion states, the accessible quartets are also expected to be unstable with respect to fragmentation following population at energies above 15.963 eV.[83] Furthermore, quartet states accessed below the first dissociative ionisation limit may also contribute to the SO^+ spectrum were they to absorb one or more probe photons following ionisation. As for the singlet state ionisation routes, intermediate valence resonances in the triplet ionisation pathways would likely have affected the Koopmans' correlation for triplet ionisation. As always, the photoelectron band energies will be associated with the cationic threshold that electronically correlates with the last resonance prior to ionisation.

B. SO_2^+ TRPEPICO spectra analysis

Within the single-pump-photon dynamics and ionisation framework discussed in Sec. V A, we can assign the principle features of the MPI data shown in Figs. 5–7. These assignments were found to be consistent with the SO^+ TRPEPICO spectra (examples of which are shown in Fig. 8). The analysis leading to the assignments of the photoelectron bands observed in the SO_2^+ TRPEPICO spectra are discussed in detail in Subsection 2 of the Appendix.

As shown in Fig. 6, similar SO_2^+ photoelectron signals were observed throughout the 4.03–4.28 eV pump photon energy range. At the temporal overlap of the pump and probe laser fields, we see a number of features in the SO_2^+ photoelectron spectra with energetic cut-offs defined by the total energy available for $[1+3']$, $[2+2']$, and $[1+4']$ excitation processes leading to the $(\tilde{X})^2A_1$ cationic ground state. In

the majority of cases, the [1+3′] feature dominates the spectra with these features being most obvious with parallel laser polarisation vectors. Based on the pump photon energy dependence, polarisation dependence, and temporal profiles of these signals, they are attributed to non-resonant ionisation of SO_2 at the peak of the imposed laser fields.

At later delay times, a single long-lived photoelectron band with a kinetic energy of ∼0.55 eV dominates the SO_2^+ TRPEPICO spectra (see Figs. 7(d) and 7(h)). This band, occurring at kinetic energies below the [1+3′] energetic threshold, will be, from here on, referred to as band (1). Band (1), is attributed to resonantly enhanced ionisation of the $(\tilde{B})^1B_1$ and potentially the $(\tilde{a})^3B_1$ diabatic states. The ionisation pathway is ascribed as [1+2′+1′] leading to the $(\tilde{X})^2A_1$ cation state via the intermediate $\tilde{G}$ and, perhaps, the $\tilde{g}$ Rydberg states. Based on the polarisation dependence of the band and an associated feature in the SO^+ TRPEPICO spectrum, it appears that this signal has a secondary component due to ISC to the $(\tilde{c})^3B_2$ state and [1′+3′] ionisation leading to the dissociative $(\tilde{C})^2B_1$ cation state. The subsequent fragmentation of the $(\tilde{C})^2B_1$ cation state is thought to give rise to peak (2) at ∼0.7 eV in the SO^+ TRPEPICO spectra. The arguments leading to these conclusions are presented in Subsection 2 a of the Appendix. A schematic summary of the ionisation processes that are thought to lead to SO_2^+ photoelectron band (1) is shown in Fig. 9.

In addition to band (1), at least three other, less-intense long-lived photoelectron bands are observed in the SO_2^+ TR-PEPICO spectra. These higher-kinetic energy photoelectron bands occur above the [1+3′] energetic threshold at ∼1.3–1.6 eV, ∼2.8 eV, and ∼3.7 eV and are predominantly associated with [1+4′] ionisation. These features are highlighted in Figs. 7(d) and 7(h) and are labelled as bands (2), (3), and (1′), respectively. The temporal profiles of these bands are shown for the 4.12 eV pump photon energy experiments on the right-hand side of Figs. 7(a) and 7(e) for the high and low pump beam intensity regimes, respectively.
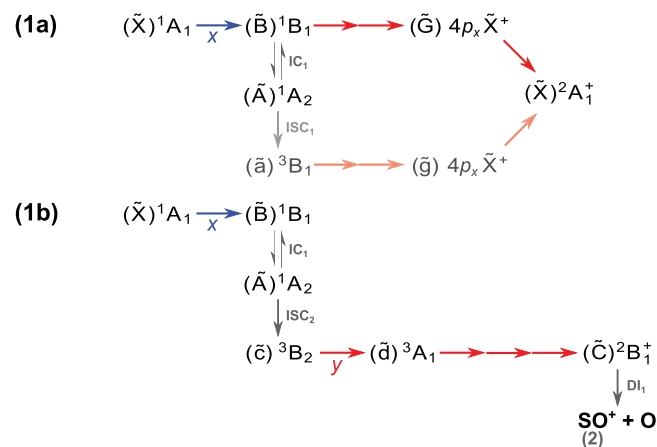

FIG. 9. Schematic of the excitation processes associated with band (1) (∼0.35–0.75 eV) in the SO_2^+ TRPEPICO spectra. Pump photon absorption is marked with blue arrows while probe photon absorption is designated by red arrows. Gray arrows highlight changes of diabatic electronic character (IC) and relativistic, spin-changing (ISC) interactions. The arrow labelled "DI" highlights a dissociative ionisation process occurring from an unstable SO_2^+ state. The number under the SO^+ fragment indicates that this process gives rise to that band in SO^+ TRPEPICO spectra.
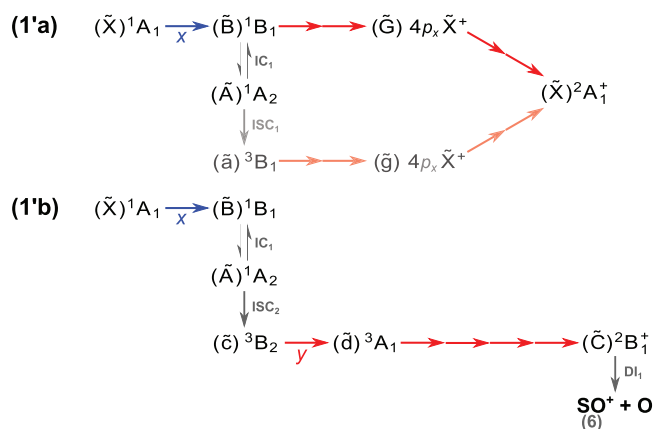

FIG. 10. As Fig. 9 but for the (1′) band.

Band (1′) is noted to exhibit similar features to band (1). Its appearance energy, ∼3.1 eV (the probe photon energy) above band (1), and its temporal behaviour suggest that it is formed through [1+4′] and [1+1′+4′] processes through similar mechanisms as those associated with band (1). A schematic summary of the ionisation processes that are thought to lead to SO_2^+ photoelectron band (1′) is presented in Fig. 10.

Band (2) may be associated with one or more possible ionisation processes occurring from low bond angle regions of configuration space. We assign band (2) to a combination of [4′] ionisation of the $(\tilde{A})^1A_2$ and potentially the $(\tilde{b})^3A_2$ states leading to the $(\tilde{C}')^2B_1$ cation state and [4′] ionisation of the $(\tilde{c})^3B_2$ state leading to the $(\tilde{a})^4A_1$ cation state. Corresponding features in the SO^+ TRPEPICO spectra, peaks (4) and (3), support these assignments. Viable explanations for the band (2) spectral features are summarised in the schematic shown in Fig. 11. The arguments used to arrive at these conclusions are discussed in Subsection 2 d of the Appendix.
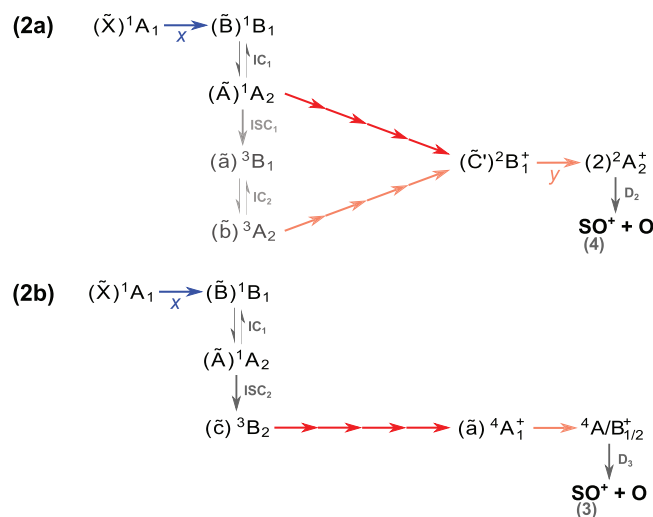
FIG. 11. As Fig. 9 but for band (2). The arrows labelled "D" highlight the single-probe-photon absorption of a cation state produced through MPI. Such excitation processes produce unstable cation states with the resulting photodissociation correlating some of the photoelectrons associated with the initial MPI process with SO^+ fragment ions. The numbers under the SO^+ ions in the figure relates the ion photodissociation process to specific bands in the SO^+ TRPEPICO spectra (see Fig. 8).

(3a) $(\tilde{X})^1A_1 \xrightarrow{x} (\tilde{B})^1B_1$

$\downarrow IC_1$

$(\tilde{A})^1A_2 \longrightarrow nl\,\tilde{A}^+$

$\downarrow ISC_1$

$(\tilde{a})^3B_1 \qquad\qquad (\tilde{A})^2B_2^+$

$\downarrow IC_2$

$(\tilde{b})^3A_2 \longrightarrow nl\,\tilde{A}^+$

(3b) $(\tilde{X})^1A_1 \xrightarrow{x} (\tilde{B})^1B_1$

$\downarrow IC_1$

$(\tilde{A})^1A_2 \xrightarrow{x} (\tilde{C})^1B_2 \longrightarrow nl\,\tilde{B}^+$

$\downarrow ISC_2 \qquad\qquad (\tilde{B})^2A_2^+ \xrightarrow{y} (\tilde{C})^2B_1^+$

$(\tilde{c})^3B_2 \longrightarrow \longrightarrow nl\,\tilde{B}^+ \qquad\qquad\qquad \downarrow D_1$

$$\mathbf{SO^+ + O}$$
$$(5)$$

FIG. 12. As Fig. 9 but for band (3).

TABLE VI. Growth time constants extracted from global fits (0–5 eV) to some of the $^{32}SO^+$ TRPEPICO data sets recorded with different pump photon energies and relatively low pump beam intensities ($\sim 2.5 \times 10^{11}$ W cm^{-2}). Time constants are presented for parallel and perpendicular relative pump-probe laser polarisation alignments. Note the similarity of the growth time constants extracted from the low pump beam intensity $^{32}SO^+$ TR-PEPICO spectra and those extracted from the $^{32}SO_2^+$ TRPEPICO data sets (see Tables IV and V).

$\hbar\omega_{pump}$ (eV)	Parallel global fit τ_1 (fs)	Perpendicular global fit τ_1 (fs)
4.03	555^{+125}_{-100}	535^{+125}_{-95}
4.12	360^{+55}_{-45}	235^{+40}_{-35}
4.28	685^{+465}_{-220}	475^{+190}_{-120}

The 2.8 eV band, band (3), displays an energetic cut-off that suggests it is produced via ionisation to the $(\tilde{A})^2B_2$ or $(\tilde{B})^2A_2$ cationic states. We ascribe this feature to $[3'+1']$ ionisation from the $(\tilde{A})^1A_2$ and potentially the $(\tilde{b})^3A_2$ diabatic states to the $(\tilde{A})^2B_2$ cation state and $[3'+1']$ ionisation from the $(\tilde{c})^3B_2$ state to the $(\tilde{B})^2A_2$ state of the cation. $[1'+2'+1']$ ionisation routes from the $(\tilde{A})^1A_2$ state to the $(\tilde{B})^2A_2$ cation state via the $(\tilde{C})^1B_2$ state may also contribute. These ionisation processes are thought to be resonantly enhanced by a number of high-n Rydberg states at the $[1+3']$ level. Photoelectrons generated through such processes partially correlate with peak (5) in the SO$^+$ TRPEPICO spectra due to probe photon absorption by the $(\tilde{B})^2A_2$ state of the cation leading to ion fragmentation. The arguments used to arrive at these conclusions are discussed in Subsection 2 c of the Appendix. A schematic summary of the ionisation processes that are thought to lead to photoelectron band (3) is shown in Fig. 12.
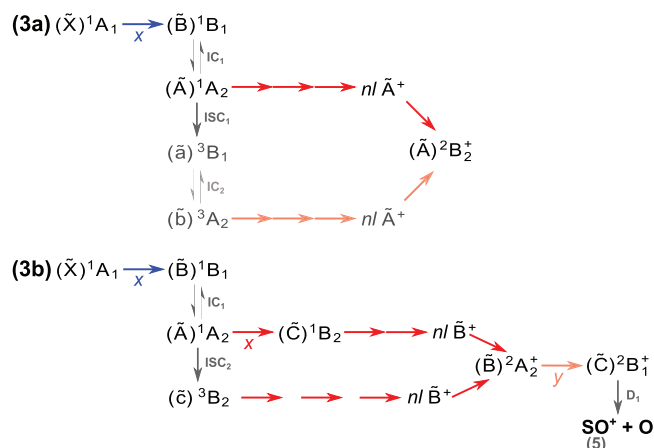
The average relaxation time constants extracted from 2D global fits to the 4.12 eV SO$_2^+$ data recorded with high and low pump intensities are summarised in Table III. For the low pump beam intensity data recorded with pump photon energies of 4.03 eV, 4.12 eV, and 4.28 eV, the results of 2D and 1D fits are summarised in Tables IV and V for parallel and perpendicular relative laser polarisations, respectively. The time constants reported in Table V are thought to be most representative of the single-pump-photon dynamics due to the applicability of simpler kinetic models (see Sec. V D). Corresponding time constants extracted from some of the low pump intensity SO$^+$ TRPEPICO data sets are shown in Table VI. As discussed in Subsection 2 of the Appendix, it is possible to attribute the band (1) signal growth component to ISC to the $(\tilde{c})^3B_2$ state. In contrast, the other SO$_2^+$ band time constants may be individually associated with IVR processes in the singlet manifold or ISC processes leading to the triplet manifold. However, we note the similar growth kinetics that are observed for the principle SO$_2^+$ photoelectron bands at all excitation energies. The signal growth kinetics observed for the low pump beam intensity SO$_2^+$ and SO$^+$ photoelectron features are also notably similar at all excitation energies. The collective implications of these observations and the band energetics are discussed in Subsection V C.

C. Single-pump-photon excited state relaxation pathways

1. Periodic motion on the $(\tilde{B})^1B_1/(\tilde{A})^1A_2$ LAS

Using the analysis reported in Sec. V B and in more detail in Subsection 2 of the Appendix, the proposed parent molecule, singlet state ionisation pathways detected using the MPI probe are overlaid on Fig. 3(a). The band (1) singlet ionisation pathway is labelled "e$^-$(1)" in this figure. The energetics of the sharp component of band (1) were found to be invariant with pump-photon energy, consistent with a Rydberg ionisation pathway. The associated "e$^-$(1)" ionisation route indicates that MPI occurs from the $(\tilde{B})^1B_1$ diabat to the $(\tilde{X})^2A_1$ ion state via the $\tilde{G}$ Rydberg state. In this principle $[1+2'+1']$ ionisation pathway, the FC factors for $[2']$ excitation to the $\tilde{G}$ Rydberg state result in a coordinate specific ionisation probability, leading to a ~ 150 fs periodic modulation of the SO$_2^+$ ion and band (1) photoelectron yield. The oscillatory time constants extracted through Fourier transformation of the different data sets are shown in Tables III–V. The periodicity of these signals are in good agreement with those expected from the experimental absorption spectrum[30] and the excited singlet state wavepacket propagation calculations of Lévêque *et al.*[28] As the ionisation process responsible for the sharp component of band (1) occurs from a specific region of the accessed coordinate space on the $(\tilde{B})^1B_1/(\tilde{A})^1A_2$ LAS, the MPI probe technique is sensitive to the periodic component of the excited state wavepacket (and any aperiodic component) that enters this probe window. This perspective is supported by the wavepacket and MPI calculations presented by Lévêque *et al.* in Paper III,[43] which reproduce the characteristic features of the oscillatory component of band (1) (band energetics and ~ 150 fs oscillatory period) and support the attribution of the oscillatory component to $[2'+1']$ MPI via the $\tilde{G}$ Rydberg state.[43] Notably, the FC window for the $[2'+1']$ ionisation process appears to be displaced in coordinate space with respect to the FC window for pump photon absorption based on the $\sim 0.2\pi$ oscillatory phase shift extracted from the SO$_2^+$ TRPEPICO spectra.

Based on the observed SO$_2^+$ and SO$^+$ ionisation energetics, higher kinetic energy bands also appear to show sensitivity to the excited state wavepacket at nuclear geometries

associated with dominant $(\tilde{A})^1A_2$ character (see Subsections 2 c and 2 d of the Appendix). Consistent with the excited state wavepacket being expected to take on dominant $(\tilde{A})^1A_2$ character within the temporal resolution (cross-correlation FWHM) of the experiments,[9,27–29] we do not appear to resolve signal growth due to the population of the optically dark $(\tilde{A})^1A_2$ state. However, we partially assign the cross-correlation limited step function temporal components of band (2) to $(\tilde{A})^1A_2$ ionisation to produce the $(\tilde{C}')^2B_1$ cation state through a $[1+3'+1']$ ionisation process. The corresponding band (2) ionisation pathway is labelled "e⁻(2)" in Fig. 3(a). Similarly, the cross-correlation limited step function component of band (3) is partially attributed to $[1+3'+1']$ ionisation of the $(\tilde{A})^1A_2$ state to produce the $(\tilde{A})^2B_2$ and/or $(\tilde{B})^2A_2$ cation state(s). The corresponding band (3) singlet ionisation pathway is labelled "e⁻(3)" in Fig. 3(a). For clarity, only the ionisation route leading to the $(\tilde{A})^2B_2$ cation state is shown in the figure.

The MPI probe process is sensitive to changes in the diabatic electronic character of the accessed neutral, intermediate, and ionic states. Hence, without knowing the position of the probe FC windows in coordinate space, we are unable to comment on non-adiabatic population transfer between the $(\tilde{B})^1B_1/(\tilde{A})^1A_2$ UAS and LAS. However, the results presented in Paper II[29] and by Lévêque *et al.*[28] suggest that the majority of the UAS population is lost within the time resolution of these experiments. As stated in the Introduction, the same calculations suggest that only small portions of the excited state wavepacket will be transferred between the UAS and LAS at later pump-probe delay times.

Multiple excited singlet and triplet states contribute to the different photoelectron bands observed with the MPI probe resulting in spectral overlap between the photoelectron features. Hence, we are unable to say anything definitive about IVR time scales within the singlet manifold. Based on the pump-probe delays over which we recorded data with high temporal resolution (−0.4 to 2.0 ps), we suggest that IVR processes either have little effect on the MPI probability or that they occur on longer time scales than were probed with high resolution here. Consistent with previous fluorescence experiments,[10,12,15,32,71] we assume that the population of the $(\tilde{B})^1B_1$ and $(\tilde{A})^1A_2$ state probed in these experiments will result in a relatively constant, long-lived offset of the ionisation signal associated with bands (1), (2), (3), and (1′) over a 0.1 to 100.0 ps pump-probe delay range. We suggest that a different component of the excited state wavepacket, that is ineffectively probed within the singlet manifold, undergoes ISC to the triplet states. This process is discussed in Subsection V C 2.

2. ISC to the triplet manifold

Three observations that were mentioned in Sec. V B (and are discussed in Subsection 2 of the Appendix) suggest that the growth time constants extracted from the low pump beam intensity TRPEPICO spectra are predominantly associated with ISC from the $(\tilde{B})^1B_1/(\tilde{A})^1A_2$ LAS. The similar growth time constants extracted from the SO_2^+ bands (1), (1′), (2), and (3) and the common pump-photon energy

dependence of these time constants (see Table V) suggest that they reflect a common relaxation process. Similar arguments also apply to the matching time constants extracted from the low pump beam intensity SO^+ TRPEPICO data (see Table VI).

At a particular pump photon energy, different degrees of vibrational excitation were prepared in the $(\tilde{B})^1B_1$ and $(\tilde{A})^1A_2$ diabatic states that are known to have dissimilar topographies. Therefore, due to different vibrational state densities and vibrational mode couplings, different IVR rates would be expected within these diabatic states. On this basis, if the signal growths were attributable to IVR leading to different ionisation FC windows on the singlet LAS, different growth time constants would be expected for the photoelectron bands associated with ionisation from the two different diabats. Using similar arguments, we would also expect the variation of the pump photon energy to have a disparate effect on the growth time constants extracted from the photoelectron bands associated with the two singlet diabatic states. The similarity of the growth time constants and their pump photon energy dependence, therefore, implies that the signal growth is not associated with IVR but an alternative relaxation process. We suggest that the measured growth time constants reflect the ISC rate coefficients.

The marked polarisation dependence of the band (1) and band (1′) temporal profiles can only be readily explained through resonant ionisation of the $(\tilde{c})^3B_2$ state via the $(\tilde{d})^3A_1$ state (see Subsection 2 a of the Appendix). Other, similarly polarised transitions from the one-pump-photon accessible states would not lead to photoelectrons with kinetic energies consistent with bands (1) and (1′). This suggests that the $(\tilde{c})^3B_2$ state is populated on an ultrafast time scale and that this process is responsible for the growth component of band (1). We note that photoelectron bands (2) and (3) occur within close energetic proximity of ion state thresholds associated with removal of a single electron from the dominant electronic determinant of the $(\tilde{c})^3B_2$ state. Hence, the similar growth time constants associated with the different photoelectron bands, at all of the pump photon energies implemented, suggest that the photoelectron signal growths are primarily attributable to ISC from the singlet LAS to the $(\tilde{c})^3B_2$ state. This conclusion is supported by the results presented in Paper II[29] and the results of Lévêque *et al.*[34] Using the results of this analysis, we constructed the triplet ionisation pathway summary shown in Fig. 3(b).

The pathway labelled "e⁻(1)" in Fig. 3(b) highlights the ISC process thought to occur to the $(\tilde{c})^3B_2$ state and the $[1'+3']$ ionisation route to the $(\tilde{C})^2B_1$ state. This process is thought to be resonantly enhanced by the $(\tilde{d})^3A_1$ state with the growth component of photoelectron band (1) corresponding to the population rate of the $(\tilde{c})^3B_2$ state. An alternative, polarisation independent, triplet $[3'+1']$ ionisation route from the $(\tilde{a})^3B_1$ state to the $(\tilde{X})^2A_1$ state via the $\tilde{g}$ Rydberg state is also shown. The rate of population of the $(\tilde{a})^3B_1$ state may also affect the extracted growth time constant (although the results reported in Paper II[29] and by Lévêque *et al.*[34] suggest that this is a minor ISC route). The time scale of the ISC and ionisation processes associated with ionisation pathway (1) in Fig. 3(b) were found to vary between 415^{+120}_{-80} fs, 205^{+70}_{-60} fs,

and 315^{+75}_{-65} fs following excitation at 4.03 eV, 4.12 eV, and 4.28 eV, respectively. In the same figure, a $(\tilde{c})^3B_2$ state ionisation pathway associated with band (2), labelled "e⁻(2)," is shown. This signal is attributed to $[1+3'+1']$ ionisation from the $(\tilde{c})^3B_2$ state to the $(\tilde{a})^4A_1$ state from a low-bond angle, extended bond length nuclear geometry. The associated signal growth time constants varied between 490^{+130}_{-95} fs, 220^{+50}_{-40} fs, and 390^{+165}_{-105} fs following excitation at 4.03 eV, 4.12 eV, and 4.28 eV, respectively. The band (3) component that is predominantly attributed to ISC to the $(\tilde{c})^3B_2$ state is described by the "e⁻(3)" pathway in Fig. 3(b). The band (3) time constants thought to correspond to population of the $(\tilde{c})^3B_2$ state and ionisation leading to the $(\tilde{B})^2B_2$ cation state varied between 540^{+180}_{-120} fs, 240^{+105}_{-75} fs, and 410^{+365}_{-170} fs following excitation at 4.03 eV, 4.12 eV, and 4.28 eV, respectively. All of these assignments are supported by the energetic positions of the discrete photoelectron features in the SO⁺ TRPEPICO spectra and the similar growth time constants extracted from the low pump beam intensity SO_2^+ and SO⁺ data sets (see Subsection 2 of the Appendix).

Despite the analysis reported above favouring the predominant population of the $(\tilde{c})^3B_2$ state, previous experiments have highlighted coupling between the Clements bands and the $(\tilde{a})^3B_1$ state.[15,32,71] Paper II[29] and the results of Lévêque *et al.*[34] suggest that the ISC process from the $(\tilde{A})^1A_2$ state does occur to the $(\tilde{a})^3B_1$ state, albeit with reduced yield and on an increased time scale with respect to ISC to the $(\tilde{c})^3B_2$ state. A recent publication by Xie *et al.* suggests that the $(\tilde{a})^3B_1$ state is significantly populated on a ~300 fs time scale from the $(\tilde{A})^1A_2$ diabatic state.[97] However, the ISC pathway to the $(\tilde{c})^3B_2$ state was not considered in the theoretical treatment of Xie *et al.*[97] Given the proposed importance of this state in the Clements band relaxation dynamics, the yield for $(\tilde{a})^3B_1$ population and the rate of appearance of this population are likely overestimated in the work of Xie *et al.*[97] As discussed in Subsection 2 of the Appendix, singlet IVR and a minor ISC route to the $(\tilde{a})^3B_1/(\tilde{b})^3A_2$ manifold could affect the photoelectron band temporal profiles. Any differences in the time constants associated with the SO_2^+ bands (1), (1'), (2), and (3) may, therefore, be related to differing contributions of three unresolved relaxation processes; IVR on the singlet LAS, ISC from the $(\tilde{A})^1A_2$ state to the $(\tilde{a})^3B_1$ state and the dominant ISC relaxation pathway leading to the $(\tilde{c})^3B_2$ state. A similar explanation could also partially account for the polarisation dependence of the low-pump intensity time constants (see Tables IV and V). However, the pump photon energy and polarisation dependences of the time constants could also be accounted for by FC windows for ionisation being reached on different time scales on the $(\tilde{c})^3B_2$ state following excitation at different pump photon energies and/or probing with different relative laser polarisations. Hence, any sensitivity to ultrafast singlet IVR and/or an ISC pathway leading to the $(\tilde{a})^3B_1/(\tilde{b})^3A_2$ manifold in these measurements cannot be confirmed.

We also consider the role of spin-orbit coupling mediated transfer from the $(\tilde{c})^3B_2$ state to the coupled $(\tilde{a})^3B_1/(\tilde{b})^3A_2$ manifold. Based on the TRPEPICO results, there is no evidence for such a sequential ISC process. However, we note that if population were to transfer between the three triplet states on a multi-picosecond time scale, we would not be sensitive to such processes in the experiments reported here. Furthermore, signatures of ionisation of the $(\tilde{a})^3B_1$ and $(\tilde{b})^3A_2$ states are expected to overlap with features attributed to $(\tilde{c})^3B_2$ state ionisation (see Subsection 2 of the Appendix). Therefore, these MPI experiments are unlikely to show a high sensitivity to the triplet-triplet transfer processes unless the ionisation cross-sections for the different triplet states are significantly different. Given the ~7 meV $(\tilde{c})^3B_2$ to $(\tilde{a})^3B_1/(\tilde{b})^3A_2$ spin-orbit coupling matrix element amplitudes extracted from the electronic structure calculations and the degeneracy of the triplet diabats at accessible regions of coordinate space (corresponding to maximum triplet-to-triplet transfer time constants of ~300 fs), ultrafast population transfer may occur within the triplet manifold. However, we note that such processes were found to have minor yields in the surface-hopping calculations reported in Paper II.[29]

As ISC is a relativistic effect, enhanced by the electronic motion in the vicinity of the second row sulfur atom, the $(\tilde{B})^1B_1/(\tilde{A})^1A_2$ to $(\tilde{c})^3B_2$ ISC time scales reported here should be unsurprising. These time constants are consistent with the magnitudes of the spin-orbit coupling matrix elements obtained from the electronic structure calculations (~10 meV corresponding to maximum ISC rates of the order of 200 fs⁻¹), the results reported in Paper II[29] and the results of Lévêque *et al.*[34] The lack of alternative ultrafast, spin-allowed relaxation processes within the Clements manifold and the degeneracy of the singlet and triplet potential energy surfaces at regions of coordinate space that are readily explored by the excited state wavepacket lead to optimal conditions for efficient ISC. We note that the specifics of this ISC process, including the pump photon energy dependence of the ISC time constants, can only be determined through wavepacket propagation calculations based on accurate, spin-orbit interaction corrected potential energy surfaces.

Additionally, the degree of ISC to the $(\tilde{c})^3B_2$ state cannot be determined from the current measurements. The MPI probe likely interrogates specific, and as yet undetermined, regions of the $(\tilde{c})^3B_2$ coordinate space. The resonantly enhanced ionisation cross-sections from this state to the correlated ion manifolds are also unknown. However, the combination of the results reported here, those presented in Paper II[29] and those of Lévêque *et al.*,[34] suggest that the ISC pathway to the $(\tilde{c})^3B_2$ state is of primary importance. Therefore, we propose that a number of previous works likely detected signatures of the singlet LAS to $(\tilde{c})^3B_2$ ISC pathway. These spin-changing transitions were likely the cause of the Zeeman splitting observations of Douglas,[3] Kullmer and Demtröder,[24] and Watanabe *et al.*[17,18,33] as well as the magnetic rotation spectra recorded by Kusch and Loomis.[2] Were ultrashort pulses of significantly higher energy probe photons available (~14 eV, ~89 nm), it may be possible to learn more about the nature of the ISC processes, their relative yields and the correlated quartet ion states in a $[1+1']$ ionisation TRPES experiment. However, the spectral congestion associated with ionisation of up to five vibrationally excited neutral states leading to five or more different cation states may still make the peak analysis and identification of specific ISC channels challenging.

TABLE VII. Growth time constants extracted from global fits to some of the $^{32}SO^+$ TRPEPICO data sets recorded with different pump photon energies and parallel relative pump-probe laser polarisations. Time constants were extracted from high and low pump beam intensity data sets ($\sim 1.0 \times 10^{12}$ W cm^{-2} and $\sim 2.5 \times 10^{11}$ W cm^{-2}, respectively). Reduced time constants were extracted for the high pump beam intensity data sets in most cases. This effect is interpreted as a signature of two processes contributing to the SO$^+$ TRPEPICO spectra when higher pump beam intensities are implemented (two-pump-photon dissociation occurring on a faster time scale than the dissociative ionisation/post ionisation absorption and dissociation processes predominantly observed at low pump beam intensities). The interplay of these processes are discussed in Sec. V D of the main body of the text.

$\hbar\omega_{pump}$ (eV)	High pump intensity fit τ_1 (fs)	Low pump intensity fit τ_1 (fs)
4.03	410^{+160}_{-100}	555^{+125}_{-100}
4.12	320^{+85}_{-65}	360^{+55}_{-45}
4.28	425^{+90}_{-65}	685^{+465}_{-220}

D. Interference from two-pump-photon excited state relaxation pathways

The effects of two-pump-photon absorption have been investigated through the pump beam intensity and relative laser polarisation dependence of the SO$_2^+$ and SO$^+$ TRPEPICO spectra. Signatures of this process are seen through comparison of the high and low pump beam intensity data shown in Figs. 5–8 and Tables III and VII. Generally, complex kinetics were observed in the SO$_2^+$ TRPEPICO spectra when high pump beam intensities were implemented. Complex temporal profiles were also observed in some of the lower pump beam intensity SO$_2^+$ data sets when parallel relative laser polarisations were implemented (see Table IV). We were unable to accurately fit the associated experimental data due to the coupled nature of multiple time constants occurring within the same decade and the limited statistics afforded by these coincidence measurements. In the case of perpendicular relative laser polarisations and higher pump beam intensities, seemingly simpler kinetic models could be applied. In these cases, faster time constants were always extracted from the high pump beam intensity data with respect to the lower pump beam intensity data sets. These findings suggest that a higher-order pump photon process leads to transient low-energy (0–4 eV) photoelectrons that correlate with SO$_2^+$ and overlap with signatures of the single-pump-photon dynamics. Based on the SO$^+$ TRPEPICO spectra and previous TRMS studies,[38,39] we suggest that the transient SO$_2^+$ photoelectron signals are attributable to two-pump-photon excitation to doubly electronically excited states. One of these doubly excited states leads to vibrationally excited levels of the $(\tilde{B})^1B_1/(\tilde{A})^1A_2$ LAS through internal conversion with the vibrationally excited molecules subsequently dissociating. Some of the resulting neutral SO fragments are thought to be selectively ionised through resonantly-enhanced MPI with the associated photoelectrons contributing to the high pump beam intensity SO$^+$ TRPEPICO spectra. A schematic summary of these processes and the resulting ionisation dynamics is shown in Fig. 13. A justification for this interpretation is given below.
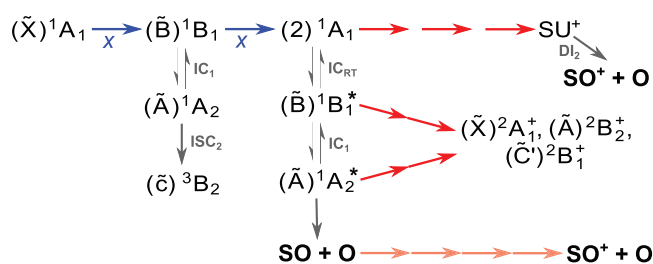

FIG. 13. As Fig. 9 but for the two-pump-photon processes occurring following high intensity laser pumping. The IC$_{RT}$ arrows highlight the Renner-Teller internal conversion process between the $(2)^1A_1$ and $(\tilde{B})^1B_1$ states. The "starred" state labels indicate highly vibrationally excited electronic states and SU$^+$ represents a collection of high-lying doubly and potentially triply excited, (pre)dissociative ion states.

Two-pump-photon absorption would have accessed the energetic window associated with the broad 7.5–8.5 eV ($\sim$170–150 nm) absorption region that is referred to in single photon absorption as the $\tilde{E}$ band.[87,88,95] In single-photon absorption experiments, this absorption profile is thought to be associated with excitation to a number of the six or more singlet states that occur in this energetic window[87,95] (labelled states "$\tilde{E}$" in Fig. 3(a)). In two-photon absorption experiments, resonantly enhanced absorption pathways will dominate. With the initial excitation to the $(\tilde{B})^1B_1$ state being x-polarised, further x-polarised excitation will be favoured by the linearly polarised, ultrashort pump pulses implemented here. Considering the dominant electronic characters of the accessible states from either the $(\tilde{B})^1B_1$ or quickly accessed $(\tilde{A})^1A_2$ states, only the $(2)^1A_1$ $((8a_1)^0(3b_1)^2$-$(2b_1)^1(3b_1)^1$ dominant electronic character at the ground state equilibrium geometry) and $(2)^1B_2$ $((5b_2)^1(8a_1)^1(3b_1)^2)$ states could be accessed via x-polarised transitions. Furthermore, the transitions from the $(\tilde{B})^1B_1$ state to the $(2)^1A_1$ state and the $(\tilde{A})^1A_2$ state to the $(2)^1B_2$ state are the same single-electron transitions that occurred in the initial $(\tilde{X})^1A_1$ to $(\tilde{B})^1B_1$ excitation. Therefore, the energy of the $(2)^1A_1$ and $(2)^1B_2$ states can be assumed to be in resonance with two pump photons when the electron configuration interaction is ignored. In the case of the $(2)^1A_1$ state, this assumption is supported by a number of multireference electronic structure calculations.[8,87,93,95]

The adiabatic $(2)^1A_1$ state of SO$_2$ forms a Renner-Teller pair[98,99] with the $(\tilde{B})^1B_1$ state, becoming degenerate and having $^1\Pi_u$ symmetry at linear geometry.[8,93] We note that the $(2)^1A_1$ state is unstable at the ground state equilibrium geometry, having a potential gradient leading to linearity along the bond angle coordinate (see Fig. 3(a)). The $(2)^1A_1$ $((3)^1A')$ state is also unstable along the asymmetric stretch coordinate with only a slight barrier to adiabatic dissociation occurring due to an avoided crossing with the $(3)^1A_1$ $((4)^1A')$ state.[8,93] As the two-pump-photon process can populate states at an energy in excess of the first ten dissociation limits of SO$_2$,[35,36,100–102] the $(2)^1A_1$ state is expected to fragment via number of pathways. These processes are expected to lead to a photoproduct distribution of SO and O fragments that covers a large range of possible rovibronic states.[37] In the experiments reported here, a subset of the SO photoproducts are thought to be ionised through [3′] or [4′] resonantly enhanced probe

processes with the resulting photoelectrons contributing to the high pump beam intensity SO^+ data shown in Figs. 8(a)–8(c).

All of the accessible diabatic electronic states that were populated at the one-pump-photon level could be accessed at the two-pump-photon level with significantly increased vibrational energies due to the Renner-Teller interaction between the $(2)^1A_1$ adiabatic state and the $(\tilde{B})^1B_1/(\tilde{A})^1A_2$ LAS. With >4 eV of internal energy, these states would dissociate. Were these vibrationally excited states to be ionised prior to dissociation, transient signals would be expected in the SO_2^+ TRPEPICO spectra that could overlap with the single-pump-photon SO_2^+ photoelectron signals. The two-pump-photon excited states accessed with ultrashort pulses at similar pump photon energies as those implemented here were found to fragment on a ~200–300 fs time scale through the TRMS experiments of Knappenberger *et al.*[38] and Zhang *et al.*[39] Therefore, at the highest pump beam intensities implemented in our experiments, transient photoelectron signals may be expected to appear at early pump-probe delays in the SO_2^+ TRPEPICO spectra. These signals would have growth components associated with the Renner-Teller induced internal conversion time (on a time scale comparable to the temporal resolution of the TRPEPICO experiments) and decay components associated with the dissociation time of the vibrationally excited states. These two processes should lead to neutral fragmentation time constants that are similar to those extracted in the previous TRMS experiments. SO^+ appearance times of ~320–430 fs were generally extracted from the high-pump intensity $^{32}SO^+$ TRPEPICO data reported here (see Table VII). In general, larger time constants were extracted from the SO^+ data sets associated with the lower pump beam intensity data. This pump beam intensity dependence of the time constants suggests that there are two processes contributing to the high pump beam intensity SO^+ TRPEPICO signal growths, relatively fast two-pump-photon dissociation with MPI of a subset of the fragments and ISC followed by dissociative ionisation. Therefore, transient, intensity dependent signals are expected to overlie the signals associated with the single-pump-photon dynamics in the SO_2^+ and SO^+ TRPEPICO spectra. The pump beam intensity dependence reported here should allow us to observe signatures of such two-pump-photon signals.

Through the $(2)^1A_1$-$(\tilde{B})^1B_1$ Renner-Teller interaction, we expect that all of the SO_2^+ photoelectron bands discussed in Sec. V B will be affected to a degree by the states accessed at the level of two pump photons when high pump beam intensities are implemented. This view is supported by the decrease of some of the extracted time constants at higher pump beam intensities and the onset of complex (multiexponential growth and decay) temporal behaviour for certain photoelectron bands (see Tables III and IV). We interpret these effects as signatures of the ionisation of the transient, vibrationally excited molecules in the $(\tilde{B})^1B_1$ state, and readily produced highly vibrationally excited $(\tilde{A})^1A_2$ state to produce low-lying, stable cation states (predominantly $(\tilde{X})^2A_1$, $(\tilde{A})^2B_2$, and $(\tilde{C}')^2B_2$). The resulting signal decay behaviour overlaps with the one-pump-photon produced long-lived signals that were associated with the $(\tilde{B})^1B_1$ and $(\tilde{A})^1A_2$ states, any oscillatory signals observed (see Sec. V C 1) and the signal

growth components ascribed to the ISC process (see Sec. V C 2). Depending on the relative contributions of the growth and decay signals to the SO_2^+ TRPEPICO spectra, complex or seemingly simple kinetic profiles may be observed.

Considering the effects of two-pump-photon excitation and the dissociative ionisation processes discussed in Subsection 2 of the Appendix and Secs. V B and V C 2, we would also expect multicomponent time constants in the high pump beam intensity SO^+ TRPEPICO spectra. In this case, growth components would be associated with two-pump-photon neutral dissociation and fragment MPI as well as neutral ISC and parent ionisation leading to unstable cation states. The contributions of the neutral SO fragments, produced through two-pump-photon absorption, to the SO^+ TRPEPICO spectra will depend on the nature of the photoproduct distribution formed by our ultrashort pump pulses. Were similar two-pump-photon photoproduct distributions formed as those measured using nanosecond lasers by Effenhauser *et al.*,[37] we may expect a photoproduct distribution predominantly made up of a 1:1 ratio of $SO(X^3\Sigma^-)$ ($T_0 = 0$ eV) and $SO(a^1\Delta)$ ($T_0 = 0.797$ eV[100]) fragments formed in a wide range of rovibrational states. We highlight the increased SO^+/SO_2^+ ratio observed as higher pump beam intensities were implemented (see Fig. 4) and the increased intensity of peak (5) and the reduced contrast of peak (3) in the SO^+ TRPEPICO DAS shown in Fig. 8(c) with respect to Fig. 8(f). When the first ionisation potential of SO (10.294 eV or 120.44 nm for $SO^+(X^2\Pi_{\frac{3}{2}})$ production[79]) is considered along with the excess energy associated with the two-pump-photon photodissociation (~2.39/2.57/2.89 eV for 4.03/4.12/4.28 eV pump photon energies), the increased SO^+ TRPEPICO signals around peaks (3) and (5) are consistent with a subset of the SO fragments being [3'] and [4'] resonantly ionised. Furthermore, the observation of SO^+ yields in excess of the SO_2^+ yields when high pump beam intensities are implemented would be difficult to explain based on the ionisation, subsequent ion state absorption and dissociation processes discussed in Subsection 2 of the Appendix. Post ionisation absorption and fragmentation mechanisms have to result in SO_2^+ yields in excess of the SO^+ yields when the probability of SO_2^+ probe photon absorption is considered. This implies that there are additional sources of SO^+ ions in our high pump beam intensity experiments, i.e., two-pump-photon induced neutral dissociation and selective MPI of the SO fragments.

We note the similarity of the time constants associated with ISC and the two-pump-photon dissociative processes. The temporal profiles associated with ISC (~200–550 fs SO^+ signal growth) at low pump beam intensities and mixed ISC/Renner-Teller facilitated two-pump-photon dissociation (~315–425 fs SO^+ signal growth) at high pump beam intensities are overlaid by oscillatory components in the SO_2^+ TRPEPICO data sets. Therefore, it is not surprising that we cannot meaningfully fit these complex temporal behaviours and that we are unable to decompose them into their constituent parts. In the previously reported TRMS results of Knappenberger *et al.*[38] and Zhang *et al.*,[39] higher pump beam fluences were likely implemented than in the experiments described here, leading to increased contributions of the two-pump-photon initiated dynamics in their experiments.

Two-pump-photon accessed excited state lifetimes of 220–280 fs were extracted from the SO_2^+ ion yield decay profiles with matching SO^+ ion growth time constants observed. These SO_2^+ signal decays suggest that the two-pump-photon decay kinetics likely dominated over the expected growth signals associated with one-pump-photon excitation and ISC in the experiments of Knappenberger *et al.*[38] and Zhang *et al.*[39] The general reduction of the growth time constants extracted in the TRMS experiments with respect to the ISC time constants extracted here support the interpretation that the high pump beam intensity TRPEPICO data have a higher relative sensitivity to the ISC process than the previous TRMS experiments. However, these high pump beam intensity TRPEPICO data sets also appear to show some signatures of two-pump-photon dissociation. In contrast, at low pump beam intensities, the TRPEPICO experiments appear to be predominantly sensitive to the ISC process. This is inferred based on the applicability of simple kinetic models and the self consistency of the SO_2^+ and SO^+ TRPEPICO growth time constants.

The fact that the complex temporal behaviour seems to be more readily observed in the SO_2^+ TRPEPICO spectra with parallel relative laser polarisations (see Tables IV and V) suggests that the transient, highly vibrationally excited $(\tilde{B})^1B_1$ and $(\tilde{A})^1A_2$ states are more efficiently probed in these cases. Here the increased vibrational energy in these states may open alternative intermediate resonances for ionisation that favour parallel relative laser polarisations. With such high degrees of internal energy and the mixed electronic character of the states accessed, multiple routes to multiple cation states would become accessible. Regardless of the ionisation routes associated with the two-pump-photon transients, their attribution to the Renner-Teller interaction between the $(2)^1A_1$ and $(\tilde{B})^1B_1$ states suggests that they will likely interfere with the observation of the single-pump-photon dynamics whenever an experiment is sensitive to diabatic electronic characters. This will be particularly true when high pump intensities, ultrashort pump pulses and/or less-differential probe techniques are implemented.

VI. CONCLUSIONS

We have presented a time domain description of the excited state dynamics occurring following Clements band excitation based on the extensive literature and the original experimental and theoretical results reported here. Using the TRPES and TRPEPICO techniques and a MPI probe scheme, we have observed ultrafast non-adiabatic and ISC dynamics occurring on similar time scales in SO_2 at different levels of excitation. Through the SO_2^+ TRPEPICO spectra, signatures of the periodic wavepacket motion responsible for the Clements band structure have been observed. These results are consistent with the singlet state MPI calculations presented in Paper III.[43] Both singlet and triplet neutral electronically excited states are thought to contribute to all of the photoelectron bands observed in the SO_2^+ TRPEPICO spectra. Through pump photon energy and relative laser polarisation studies of the low pump beam intensity SO_2^+ and fragment SO^+ TRPEPICO spectra, we have assigned the dominant MPI probe mechanisms and inferred that ISC

occurs from the $(\tilde{B})^1B_1/(\tilde{A})^1A_2$ LAS on a sub-picosecond, pump photon energy dependent time scale. These results suggest that the $(\tilde{c})^3B_2$ state is the predominantly populated triplet state, in agreement with the results presented in Paper II[29] and by Lévêque *et al.*[34] Following excitation to the Clements C and D bands, ~400–700 fs growth time constants were measured and primarily attributed to this ISC process. These time constants were observed to reduce to ~150–350 fs following excitation to the Clements F and G bands, whereas, ISC time constants between ~250–750 fs were extracted after excitation to the Clements N, N′ and O bands. These time constants are consistent with the calculated spin-orbit coupling matrix element amplitudes and the results reported in Paper II[29] and by Lévêque *et al.*[34]

The effects of dissociative two-pump-photon excited states on the observation of the single-pump-photon dynamics have been highlighted through the coincident detection of electrons with the parent and the dominant SO^+ photofragment ions. The contribution of the two-pump-photon excited states to the parent ion signals were recognised through relative laser polarisation and pump beam intensity studies. The consequences of these transient states, thought to be readily accessed at the level of two-pump-photons, have been discussed.

Coupled with dynamics calculations incorporating accurate non-adiabatic and spin-orbit coupling treatments, it is hoped that the results reported here will facilitate a more complete understanding of the Clements band excited state dynamics. More generally, these results emphasise the utility of the TRPEPICO technique and multireference electronic structure methods to provide perspicacity in complex excited state non-adiabatic and spin-changing processes.

APPENDIX: DETAILED ANALYSIS OF THE TIME-RESOLVED PHOTOELECTRON-PHOTOION COINCIDENCE SPECTRA

1. Supplementary electronic structure calculation results

Here we present some supplementary results from the electronic structure calculations that were helpful in the interpretation of the TRPEPICO measurements described above. Table VIII highlights the equilibrium energies and equilibrium nuclear geometries of some of the relevant neutral states whereas Table IX shows the corresponding results for the ionic states. CASSCF+MCQDPT2, C_{2v} restricted potential energy curves of some of these ionic states are shown in Fig. 14.

TABLE VIII. State symmetry labels and optimised equilibrium bond lengths, r_e, and bond angles, α_e, of the low-lying neutral states of SO_2 as determined through initial C_{2v} restricted CASSCF calculations. MCQDPT2 corrected equilibrium state energies, T_e, associated with the optimised nuclear configurations are also shown. The expected uncertainties of these values are shown in parentheses next to each datum.

State	T_e (eV)	r_e (pm)	α_e (°)
$(\tilde{X})^1A_1$	0	143.9	119.4
$(\tilde{A})^1A_2$	3.1(2)	155.4	97.0
$(\tilde{B})^1B_1$	3.5(2)	155.9	116.9
$(\tilde{a})^3B_1$	3.0(2)	152.2	124.5
$(\tilde{b})^3A_2$	3.2(2)	155.3	96.9
$(\tilde{c})^3B_2$	3.5(2)	157.2	106.9
$(\tilde{d})^3A_1$	6.1(2)	161.5	117.7

TABLE IX. Symmetries, dominant electronic characters, and T_e, r_e, and α_e values of a number of the low-lying cation states of SO_2. r_e and α_e values were determined through an initial CASSCF geometry search with the T_e energies corrected at these geometries at the MCQDPT2 level. The expected uncertainties of the T_e values are shown in parentheses next to each datum.

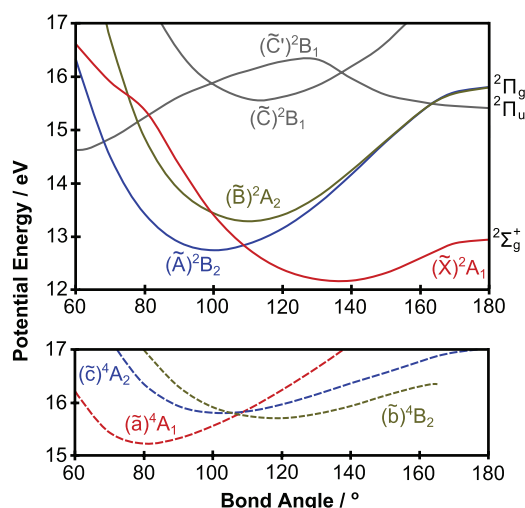| Ion state	Principle electronic determinant	T_e (eV)	r_e (pm)	α_e (°)
$(\tilde{X})^2A_1$	$(8a_1)^{-1}$	12.2(3)	144.6	128.3
$(\tilde{A})^2B_2$	$(5b_2)^{-1}$	12.7(3)	148.6	100.9
$(\tilde{B})^2A_2$	$(1a_2)^{-1}$	13.3(3)	150.1	109.7
$(\tilde{C}')^2B_1$	$(5b_2)^{-2}(3b_1)^1$	14.6(3)	159.6	60.8
$(\tilde{C})^2B_1$	$(2b_1)^{-1}$	15.6(3)	157.8	111.5
$(\tilde{a})^4A_1$	$(5b_2)^{-1}(1a_2)^{-1}(3b_1)^1$	15.3(3)	161.7	82.7
$(\tilde{b})^4B_2$	$(1a_2)^{-1}(8a_1)^{-1}(3b_1)^1$	15.7(3)	161.2	111.5
$(\tilde{c})^4A_2$	$(5b_2)^{-1}(8a_1)^{-1}(3b_1)^1$	15.8(3)	161.2	100.9

FIG. 14. Calculated bending mode potential energy curves of some of the low-lying ion states of SO_2. The curves were calculated at the CASSCF+MCQDPT2 level with a restricted C_{2v} symmetry. The symmetric stretch coordinate was optimised to the minimum energy configuration in the calculations. The doublet cation state potential energy surfaces are shown in the upper panel whereas the bending topographies of the lowest-lying quartet states are presented in the lower panel. The $(\tilde{b})^4B_2$ state potential energy curve has been truncated due to errors introduced through interactions with other states at bond angles close to linearity. These interactions are beyond the scope of this paper.

2. Photoelectron band analyses

A detailed analysis that was used to assign the individual, dominant photoelectron features in the SO_2^+ and SO^+ TRPEPICO spectra follows.

a. SO_2^+ band (1): ~0.35–0.75 eV

At early pump-probe delays (0.1–1.0 ps), band (1) clearly displays a damped oscillatory contribution with a period that approximately matches the Clements band spacings for the different excitation energies. This oscillatory feature can be seen at ~0.55 eV in the Fourier transformed TRPEPICO spectrum shown in Fig. 5(d). For this data set, recorded with a pump photon energy of 4.12 eV and a relatively high pump beam intensity, the centre of the oscillatory feature occurs at 26.5 meV with a FWHM of 9.0 meV. The centre and FWHM of the dominant feature in Fig. 5(d) corresponds to an early time (0.1–1.0 ps) oscillatory period for the recurrent portion of the excited state wavepacket of 155^{+35}_{-20} fs. Similar oscillatory periods were extracted from data recorded following excitation at 4.03 eV (145^{+30}_{-25} fs) and with different relative laser polarisations (see Table III). Data associated with the 4.28 eV pump-photon energy did not produce unique oscillatory periods so oscillatory periods are not reported for these data sets. Analogous results were obtained for data sets recorded with lower pump beam intensities (see Tables IV and V). However, single oscillatory components were less cleanly extracted through Gaussian decomposition of the energy gap profiles due to the lower signal-to-noise levels in these experiments. Based on the lifetime of band (1) as well as the oscillatory periods and their excitation energy dependence, it is clear that this dominant photoelectron band is at least partially associated with single-pump-photon excitation to the Clements bands. Considering the phase ($\sim 0.2\pi$) and period of the oscillation of band (1), we infer that the excited state wavepacket is probed close to the FC region for pump-photon absorption. This implicates ionisation from a neutral geometry associated with dominant B_1 character (see Fig. 2). The oscillatory component of band (1) highlights that the MPI probe is sensitive to the periodic wavepacket motion expected to occur on the $(\tilde{B})^1B_1/(\tilde{A})^1A_2$ LAS.[9, 27–29]

Considering the intensity and photoelectron kinetic energy of band (1) and the energetics of the ionisation process, this signal must arise from a three probe photon $[1+3']$ pathway leading to production of SO_2^+ in its $(\tilde{X})^2A_1$ ground electronic state. When the energetic position of band (1) is monitored as a function of the pump photon energy (4.03–4.28 eV), the peak position is found to be invariant (see Fig. 6). Combined with its sharp energetic profile, this strongly suggests that the dominant ionisation process is resonantly enhanced by a Rydberg state. Due to the similarity of the electronic structure of the Rydberg state and the correlated ion state, the Rydberg and cation potential energy surfaces share similar topographies. Hence, the FC factors for ionisation are highest when the vibrational energy content of the Rydberg state is preserved in the cation upon ionisation. Therefore, direct ionisation of a Rydberg state produces a sharp photoelectron band that is relatively invariant as the

internal energy of that state (and by extension that of any lower-lying state that leads to the Rydberg state) is changed. Such a process produces the sharp component of photoelectron band (1) in the SO_2^+ TRPEPICO spectra. Photoelectrons were produced with similar kinetic energies, despite the different degrees of internal excitation in the Rydberg states when the pump photon energy was changed.

Deliberating resonant enhancement by the known excited singlet electronic states of neutral SO_2 occurring close to 7.25 eV $[1+1']$[87] and 10.35 eV $[1+2']$,[87–91] a pathway via the $\tilde{G}$ $4p$ predissociative Rydberg state with an electronic term energy of 9.77 eV[89,91] seems probable. The $\tilde{G}$ state is known to converge to the ground $(\tilde{X})^2A_1$ state[91] (and hence has an $(8a_1)^1$ ion core) and has B_1 symmetry[87] associated with a p_x Rydberg orbital. Therefore, a possible explanation for band (1) would be that the 0.55 eV electron peak occurs due to two-probe-photon excitation from the $(\tilde{B})^1B_1$ state to the $\tilde{G}$ state via a relatively unpolarised transition from the $(\tilde{B})^1B_1$ diabat. This would result in ∼0.41–0.70 eV of vibrational energy in the Rydberg state depending on the implemented pump and probe photon energies. The single photon Rydberg ionisation would produce the ground cationic $(\tilde{X})^2A_1$ state with similar levels of vibrational excitation and an electron with a kinetic energy of $T_0(\tilde{G}) + \hbar\omega_{probe} - I_p(\tilde{X})$ $= 9.77 + 3.12/3.09 - 12.35 = 0.54/0.51$ eV depending on the probe photon energy. This is in good agreement with the observed peaks. The importance of this ionisation pathway in producing features consistent with band (1) is supported by the wavepacket and MPI calculations of Lévêque *et al.* that are presented in Paper III.[43]

There is also the possibility that resonant excitation could occur at the $[1+1']$ level due to a $(\tilde{C})^1B_2 \leftarrow (\tilde{A})^1A_2$ (i.e., $(5b_2)$ $\leftarrow (1a_2)$) x-polarised excitation. However, from this intermediate, a Rydberg state that correlates with the ground state of the cation could not be accessed through promotion of a single electron (see the determinants in Tables I, II, and IX). In addition, a significant phase shift would be expected in the oscillation due to the nuclear motion required to reach regions of the $(\tilde{A})^1A_2$ diabat from which such an excitation could occur. This was not observed and no other singlet states are expected to be accessible within the $[1+1']$ energy range.[87] Hence, we exclude a pathway via the $(\tilde{C})^1B_2$ state as an explanation for the sharp feature associated with band (1).

Following ISC, triplet states may also contribute to the photoelectron signals produced in coincidence with the parent ion. Considering triplet state ionisation pathways that would produce photoelectron features consistent with band (1), MPI of the $(\tilde{a})^3B_1$ $((8a_1)^1(3b_1)^1)$ diabat via a triplet Rydberg state would be likely if ISC occurred to the $(\tilde{a})^3B_1/(\tilde{b})^3A_2$ manifold. The only known Rydberg candidate for triplet ionisation in the vicinity of the $[1+2']$ excitation energy range is the $(\tilde{g})$ $4p$ state that has a term energy of 9.70 eV and correlates with the ground state of the cation.[91] This state is thought to be the triplet analogue of the aforementioned $\tilde{G}$ state and has previously been accessed in a three photon process that was resonantly enhanced by the $(\tilde{a})^3B_1$ state.[91] Therefore, a $[2'+1']$ ionisation process from the $(\tilde{a})^3B_1$ state (accessed through ISC) with resonant enhancement by the $(\tilde{g})$ $4p_x$ Rydberg state may be expected to contribute to the lower kinetic energy

side of band (1). This process would result in a photoelectron kinetic energy of ∼0.47 eV and, considering the pump and probe bandwidths, would overlap with the features associated with a singlet ionisation pathway. Based on the calculated spin-orbit coupling strengths (matrix element amplitudes up to 10 meV), the results presented in Paper II,[29] the results of Lévêque *et al.*[34] and the relatively small $\tilde{G}$-$\tilde{g}$ spin splitting, a contribution from the $(\tilde{a})^3B_1$ triplet to band (1) cannot be neglected. We note that, although many triplet states are known to be present at the implemented $[1+1']$ energies (7.12–7.40 eV),[8,87,92–95] none of these states permit a further single electron transitions that could produce molecules in the $\tilde{g}$ state. Barring ultrafast non-adiabatic processes from valence states accessed at the $[1+2']$ level leading to the $\tilde{g}$ Rydberg state, a polarisation insensitive, two-probe photon transition would be expected to occur from the $\tilde{a}$ state to the $\tilde{g}$ state.

Were ISC to occur to either of the $(\tilde{a})^3B_1$ or $(\tilde{c})^3B_2$ states, further resonantly enhanced triplet ionisation pathways could contribute to photoelectron band (1). The $(\tilde{d})^3A_1$ $((2b_1)^{-1}(3b_1)^1)$ state occurs close to the $[1+1']$ energy range and could be populated through single probe photon excitation from the $(\tilde{a})^3B_1$ or $(\tilde{c})^3B_2$ states through x- and y-polarised transitions, respectively. Absorption of three more probe photons could then produce the $(\tilde{C})^2B_1$ state of the cation and photoelectrons with energies up to 0.7 eV. Therefore, depending on the degree of ISC, the FC factors for population of the $(\tilde{d})^3A_1$ state and ionisation, these processes could contribute to an underlying component of band (1). Although there are other potential resonances at the $[1+1']$ level, the accessible states could not be projected onto ion states that would lead to photoelectron kinetic energies that are consistent with band (1).

Considering alternative triplet ionisation pathways, four probe photon ionisation routes could produce the $(\tilde{b})^4B_2$ state from either the $(\tilde{a})^3B_1$ or $(\tilde{c})^3B_2$ states. Based on the calculated $(\tilde{b})^4B_2$ ionisation potential, photoelectrons with threshold energies of ∼0.8–1.0(3) eV could be expected depending on the pump photon energy implemented. Similarly, the $(\tilde{c})^4A_2$ state could be produced via the $(\tilde{a})^3B_1$ or $(\tilde{b})^3A_2$ states through four probe photon ionisation to produce photoelectrons with kinetic energies of less than 0.7–0.9(3) eV. For these processes to result in appreciable signals, they would need to be enhanced by cation correlated Rydberg states at the $[1+3']$ level. We note that little polarisation sensitivity would be expected for these valence-Rydberg transitions due to the expected density of quartet Rydberg states of different symmetries at this level of excitation.

Summarising this section so far, band (1) may be reasonably associated with $[2'+1']$ ionisation of both the $(\tilde{B})^1B_1$ and $(\tilde{a})^3B_1$ states. $[1'+3']$ ionisation of the $(\tilde{a})^3B_1$ and $(\tilde{c})^3B_2$ states via the $(d)^3A_1$ state and $[3'+1']$ ionisation of one or more of the three triplet states may also result in contributions to band (1). Therefore, the temporal profile of this band could relate to the evolution of up to four diabatic states. With this in mind, there are a number of possible explanations of the band (1) signal growth. The temporal profile of the $(\tilde{B})^1B_1$ state signal will depend on the relative locations of the FC window for single-pump-photon absorption and two-probe-photon absorption from the $\tilde{B}$ state to the $\tilde{G}$ state. If these FC windows

overlapped, a $\tilde{B}$ state signal would have been observed immediately. However, a growth signal could be observed if nuclear motion and IVR was required to optimally populate the FC window for ionisation. An alternative explanation for the growth component arises if one or more of the triplet states were accessed and subsequently ionised. In this case, the time constant could be associated with the ISC time scale and any further nuclear motion required to reach the FC window for resonant ionisation via the relevant intermediate state.

Considering the polarisation dependence of the band (1) temporal profiles (see Fig. 5 for the 4.12 eV data set and Table III), the signal is observed with close to maximum intensity beyond the SO_2 cross-correlation signal with both parallel and magic angle polarisation geometries at all pump photon energies. However, with perpendicular relative laser polarisations, growth (denoted by negative amplitudes in the DAS shown in Fig. 7) with a pump intensity dependent time constant was observed at all pump photon energies (see Fig. 7 panels c_A, c_B, g_A, and g_B and Tables III–V). Of the resonant ionisation processes that could contribute to band (1) and have been discussed above, only one is expected to be favoured by perpendicular relative pump-probe laser polarisations. On the basis of the expected probe process polarisation sensitivities, we attribute the band (1) signal growth to population of the $(\tilde{c})^3B_2$ state and ionisation to the $(\tilde{C})^2B_1$ state of the cation via the perpendicularly polarised $(\tilde{d})^3A_1 \leftarrow (\tilde{c})^3B_2$ transition.

Support for this assignment is obtained from the low-pump beam intensity $^{32}SO^+$ TRPEPICO spectra and DAS (see Figs. 8(d)–8(f) for an example data set associated with 4.12 eV pump photons). The $(\tilde{C})^2B_1$ cation state is expected to be unstable with respect to fragmentation at the $[1+1'+3']$ level of excitation, producing SO^+ fragments following ionisation. We highlight that the most intense peaks in the low pump beam intensity SO^+ fragment TRPEPICO spectra occur at ~ 0.60 eV (see band (2) in Fig. 8(f)). These peaks are consistent with $[1+1'+3']$ ionisation of the $(\tilde{c})^3B_2$ state to produce the unstable $(\tilde{C})^2B_1$ cation state via the $(\tilde{d})^3A_1$ valence state. Furthermore, we observe that the growth time constants associated with the low pump beam intensity SO^+ TRPEPICO spectra match the low pump beam intensity SO_2^+ band (1) growth time constants where they could be extracted (see Tables IV–VI). This suggests that the low pump beam intensity SO_2^+ and SO^+ growth time constants have similar origins.

In contrast to the relative pump-probe laser polarisation dependent SO^+ time constants observed here (see Table VI), two-pump-photon neutral dissociation processes with subsequent MPI of the SO fragments would not be expected to show a high sensitivity to probe laser polarisation. With this in mind, the ~ 0.60 eV photoelectrons observed in the SO^+ TRPEPICO spectra are most likely associated with SO_2^+ ion fragmentation and SO^+ production, likely via the $(\tilde{C})^2B_1$ SO_2^+ state. The time constants extracted from the higher pump intensity data likely reflect a mixture of ISC time scales and two-pump-photon dissociation time constants (see Table VII and Sec. V D).

Consistent with all of the observations discussed above, we primarily attribute the band (1) growth component to $[1+1'+3']$ ionisation to the $(\tilde{C})^2B_1$ cation state via the $(\tilde{d})^3A_1$

state following population of the $(\tilde{c})^3B_2$ state through ultrafast ISC.

b. SO_2^+ band (1'): ~ 3.20–4.10 eV

The 3.7 eV feature, band (1'), is noted to have a very similar temporal profile to band (1) (see the dark red profile on the right-hand side of Fig. 7(a)) and is also pump-photon energy invariant. It occurs at an energy concomitant with the absorption of an extra probe photon and has a significantly reduced intensity with respect band (1). The long-lifetime of this band and its energetic position mean that it must be associated with $[1+4']$ and potentially $[1+5']$ ionisation. Therefore, we primarily associate band (1') with a $[1+2'+2']$ ionisation mechanism from the $(\tilde{B})^1B_1$ and potentially the $(\tilde{a})^3B_1$ diabatic states and $[1+1'+4']$ ionisation of the $(\tilde{c})^3B_2$ diabatic state using similar arguments to those presented in Subsection 2 a of the Appendix. The latter process would be expected to produce an unstable $(\tilde{C})^2B_1$ cation state that would fragment on our ion collection time scale.[83] Consistent with the production of such ion states, weak and broad features are observed in the SO^+ TRPEPICO spectra that span 3.2–4.2 eV (see Fig. 8(c), peak (6)).

c. SO_2^+ band (3): ~ 1.95–3.20 eV

Although band (3) is observed to be broader in energy than band (1), its energetic profile is also found to be relatively invariant with pump photon energy. These properties along with the proximity of the implemented $[1+3']$ energies to the $(\tilde{A})^2B_2$ and $(\tilde{B})^2A_2$ ionisation limits suggest that a number of closely spaced Rydberg levels are accessed with varying degrees of vibrational excitation, producing relatively high kinetic energy, pump photon energy invariant photoelectrons. The temporal profile of band (3) is shown for the 4.12 eV pump photon experiment by the blue traces on the right-hand side of Figs. 7(a) and 7(e). As a significant signal is observed for this band within the time resolution of these experiments and given the photoelectron kinetic energies that it spans, we suggest that the 2.8 eV photoelectron band is at least partially associated with resonant ionisation from the vibrationally excited, lower bond angle region of the $(\tilde{B})^1B_1/(\tilde{A})^1A_2$ LAS (with dominant $(\tilde{A})^1A_2$ character) via a Rydberg pathway.

The $(\tilde{C})^1B_2$ state $((1a_2)^1(5b_2)^2(8a_1)^2(3b_1)^1)$ is the only singlet state thought to be accessible from the singlet LAS at the $[1+1']$ level,[87] with the transition from the $(\tilde{A})^1A_2$ diabat $((1a_2)^2(5b_2)^1(8a_1)^2(3b_1)^1)$ being x-polarised. If this state was populated, absorption of two more probe photons could then excite a range of high-n $(\tilde{B})^2A_2$ Rydberg levels with differing degrees of vibrational excitation. To produce an energetic profile consistent with band (3), these levels would have to occur ~ 300 meV below the third ionisation threshold. Alternatively, a non-resonant three probe photon excitation pathway could occur from the $(\tilde{A})^1A_2$ state to a number of high-n $(\tilde{A})^2B_2$ Rydberg levels ~ 600 meV below the second ionisation limit. In this case, due to the density of Rydberg states with multiple symmetries at the $[1+3']$ level of excitation, little polarisation sensitivity would be expected. Single-photon ionisation of the Rydberg levels prepared through either of these path-

ways would produce photoelectron features consistent with band (3).

The $(\tilde{a})^3B_1/(\tilde{b})^3A_2$ triplet LAS displays a similar topography to the corresponding singlet LAS (see Fig. 3 and Paper II[29]), albeit down shifted in energy by ~400 meV (see Table I). With this in mind, we note that some portion of band (3) may also be associated with ionisation to the $(\tilde{A})^2B_2$ state from the $(\tilde{b})^3A_2$ diabat. Additionally, a further contribution to band (3) may arise due to an alternative ISC pathway leading to the $(\tilde{c})^3B_2$ state. Were this state to be ionised to the $(\tilde{B})^2A_2$ state of the cation, photoelectron features consistent with band (3) would be expected. A variety of triplet states exist at the $[1+1']$ and $[1+2']$ levels of excitation.[8,87,92–95] Due to the multitude of states and potential correlations with the $(\tilde{A})^2B_2$ and $(\tilde{B})^2A_2$ cation states, it is not currently possible to predict the polarisation dependence of ionisation of the $(\tilde{b})^3A_2$ and $(\tilde{c})^3B_2$ states. We note, however, that the time integrated yield of electrons in band (3) is relatively unaffected by changes in relative pump-probe laser polarisation. This may be due to multiple contributions to the band profile or an inherent polarisation insensitivity of the dominant ionisation routes.

In partial support for the SO_2^+ spectral assignments discussed above, the SO^+ TRPEPICO spectra shown in Fig. 8 (and the other SO^+ TRPEPICO data sets) suggest that the $(\tilde{B})^2A_2$ state is accessed following $[1+3'+1']$ excitation. Specifically, the peaks labelled (5) in Figs. 8(c) and 8(f) are consistent with the proposed parent $[1+3'+1']$ ionisation mechanism to produce $(\tilde{B})^2A_2$ cations and photoelectrons. This cation state is known to absorb at 3.1 eV[84] to produce unstable $(\tilde{C})^2B_1$ SO_2^+ via *y*-polarised transitions $(1a_2 \leftarrow 2b_1)$. The resulting cation states dissociate leading to $SO^+(X^2\Pi_\Omega)$ + $O(^3P_J)$ fragments, correlating the photoelectrons produced through MPI with the fragment ions. Consistent with such a mechanism, SO^+ peak (5) is most prominent when perpendicular relative laser polarisations are implemented. Therefore, the assignment of peak (5) in Fig. 8 to such an ionisation and cation absorption scheme provides further support for the $[1+3'+1']$ MPI assignment of SO_2^+ band (3).

Like the temporal profile of band (1), the temporal profile of band (3) exhibits a growth component. Were the $(\tilde{A})^1A_2$ state and one or more of the triplet states to contribute, a compound temporal profile would be expected. First considering the $(\tilde{A})^1A_2$ state, wavepacket calculations suggest that dominant A_2 character is acquired following excitation to the $(\tilde{B})^1B_1$ state within the time resolution of this experiment.[9,27–29] We may therefore expect a cross-correlation limited step function in the temporal profile associated with the fast population of the $(\tilde{A})^1A_2$ state and its ionisation to produce SO_2^+ in the $(\tilde{A})^2B_2$ and/or $(\tilde{B})^2A_2$ state. Depending on whether the periodic component of the excited state wavepacket passes through the FC window for ionisation, this signal may be modulated by a damped oscillation. However, were IVR on the singlet LAS required to optimally populate the FC window for $(\tilde{A})^1A_2$ ionisation, an associated growth component may also be observed in the temporal profile of band (3).

For signals associated with ionisation of the $(\tilde{b})^3A_2$ and/or $(\tilde{c})^3B_2$ states, a growth time constant would be expected due to the nuclear motion required to reach a point of ISC, the ISC rate and any further nuclear motion required to reach the FC window for ionisation. A complex temporal profile may therefore be formed and, as with band (1), high pump intensities could result in a two-pump-photon transient signal that may further complicate the temporal profile (see Sec. V D). With this in mind, analysis of band (3) alone does not allow us to definitively assign the observed signal growth to IVR on the singlet LAS or ISC to the $(\tilde{b})^3A_2$ and/or $(\tilde{c})^3B_2$ states.

d. SO_2^+ band (2): ~1.00–1.95 eV

Band (2) is most clearly observed with perpendicular relative laser polarisations due to the reduction of the intense $[1+3']$ non-resonant ionisation signal that occurs when the pump and probe fields are temporally overlapped (see Figs. 7(b) and 7(f)). In contrast to bands (1), (1') and (3), this band is found to shift with pump photon energy. The temporal profile of band (2) is shown in Figs. 7(a) and 7(e) (green traces) for the 4.12 eV pump photon energy and perpendicular relative laser polarisation case for high and low pump beam intensity conditions, respectively. As for bands (1) and (3), exponential signal growth was observed for this band (see Tables IV and V).

At excitation energies of 4.03 and 4.12 eV, the long-lived and weak band at ~1.6 eV occurs at an unusual energetic position. In these cases, band (2) occurs 0.5 eV above the $[1+3']$ $(\tilde{X})^2A_1$ adiabatic ionisation threshold and more than 1.6 eV below the $[1+4']$ threshold for production of the first three ion states. Given that band (2) shows a growth component and that the threshold for production of the $(\tilde{C})^2B_1$ ion state occurs 0.9 eV below the peak of the band, band (2) can be attributed to three possible sources.

Band (2) may be produced following relaxation to the lower bond angle region of the singlet LAS with subsequent ionisation occurring via an unknown valence state that correlates with one of the $(\tilde{X})^2A_1$, $(\tilde{A})^2B_2$ or $(\tilde{B})^2A_2$ states. In this case, the growth component of band (2) could be associated with IVR on the singlet LAS to optimally populate the FC window for excitation to the valence intermediate, likely occurring at the $[1+2']$ level. The subsequent ionisation process would have to result in 1.6 eV or more of internal energy in the cation.

Band (2) may also be attributed to ionisation leading to the electronically excited $(\tilde{C}')^2B_1$ cation state. Direct multiphoton ionisation (with potential resonant enhancement by $(\tilde{C}')^2B_1$ Rydberg states at the $[1+3']$ level) could occur to this state from the $(\tilde{A})^1A_2$ and/or the $(\tilde{b})^3A_2$ states. Such processes would be expected to produce photoelectrons with threshold energies of 1.8–2.0(2) eV depending on the pump photon energy, in good agreement with the energetic position of band (2). Considering the equilibrium geometry of the $(\tilde{C}')^2B_1$ state (see Table IX), such threshold electrons would have to be produced from low-bond angle, symmetrically stretched regions of coordinate space. In this case the band (3) signal growth could be attributed to IVR on the singlet LAS and/or ISC to reach the low-bond angle, symmetrically stretched geometries required for near threshold ionisation.

The features labelled (4) in the SO^+ TRPEPICO spectra shown in Fig. 8 are consistent with the production of $(\tilde{C}')^2B_1$ cation states at low bond angles, close to the energetic threshold. This peak suggests that the $(\tilde{C}')^2B_1$ SO_2^+ molecules absorbed a 3.1 eV probe photon to populate a higher-lying, dissociative cation state. Based on the electronic structure calculations of Li *et al.*,[96] we suggest that an additional y-polarised probe photon may be absorbed to promote the SO_2^+ cation from the $(\tilde{C}')^2B_1$ state to the dissociative[83] $(2)^2A_2$ state $((8a_1)^{-1}(5b_2)^{-1}(3b_1)^1)$ $(5b_2 \leftarrow 8a_1)$. This process would lead to the partial correlation of the $[1+4']$ photoelectrons associated with SO_2^+ band (2) with the SO^+ TRPEPICO spectrum, leading to SO^+ band (4).

Additionally, band (2) may be associated with an ionisation route leading to the quartet states of the cation from one or more of the triplet states at a relaxed, low-bond angle geometry. Based on the calculated minimum energy of the $(\tilde{a})^4A_1$ state, a $[1+4']$ ionisation scheme could be expected to produce threshold photoelectrons with kinetic energies of $\sim 1.1(3)$–$1.5(3)$ eV depending on the pump and probe photon energies, in rough agreement with the kinetic energy of photoelectron band (2). Direct ionisation could occur to the $(\tilde{a})^4A_1$ state, with potential resonant enhancement by correlated Rydberg states, from either of the $(\tilde{b})^3A_2$ or $(\tilde{c})^3B_2$ states (see Tables VIII and IX). Given the triplet state density at the $[1+1']$ level, the involvement of an intermediate triplet state in this ionisation pathway cannot be ruled out.

When the calculated $(\tilde{a})^4A_1$ state ionisation potential is considered (15.3(3) eV, see Table IX), the feature labelled (3) in the SO^+ TRPEPICO DAS shown in Figs. 8(c) and 8(f) may be associated with a $[1+4']$ parent molecule ionisation scheme. Following the production of stable $(\tilde{a})^4A_1$ cations through near threshold MPI, the cations may absorb another probe photon to produce an unstable quartet cation state of unknown symmetry. This state would be populated above the dissociative ionisation limit and would fragment on our ion collection time scale.[83] This would lead to the photoelectrons associated with $[1+4']$ MPI of the $(\tilde{b})^3A_2$ or $(\tilde{c})^3B_2$ states partially correlating with the SO^+ fragments and the associated TRPEPICO spectrum. Given the expected uncertainties of the quartet state ionisation potential calculations (± 0.3 eV), these observations are also somewhat consistent with ionisation of one or more of the three single-pump-photon accessible triplet states through absorption of four probe photons to produce the $(\tilde{b})^4B_2$ and/or $(\tilde{c})^4A_2$ cations (again, see Table IX). In either case, we highlight that the position of band (3) in the SO^+ TRPEPICO spectrum indicates that ionisation most likely occurs from a triplet state to a quartet state. Such features, attributable to ionisation to quartet cation states in both the SO_2^+ and SO^+ TRPEPICO spectra, suggest that ultrafast ISC processes occur following excitation to the Clements bands. This is in contrast to the energetics of most of the other photoelectron bands observed in these TRPEPICO measurements, as all of the other signals are also consistent with singlet state to doublet state ionisation pathways.

We note that following ISC, additional triplet ionisation pathways to the doublet ion states would be expected to occur. However, without a significant increase in internal ionic excitation, these pathways would produce photoelectron bands that would overlap with any singlet features. With this in mind, one may expect that quartet ionisation channels could provide a means of uniquely monitoring triplet state appearance. Unfortunately, the energetic threshold of the $(\tilde{C}')^2B_1$ state occurs at a similar energetic threshold as that associated with the $(\tilde{a})^4A_1$ state. The $(\tilde{b})^4B_2$ and $(\tilde{c})^4A_2$ $[1+4']$ ionisation thresholds are calculated to occur at the energy associated with ionisation of the $(\tilde{B})^1B_1$ state to the $(\tilde{X})^2A_1$ state via the $(\tilde{G})$ $4p_x\tilde{X}$ Rydberg. This prevents the unique identification of ISC signals using our MPI probe.

As can be inferred from Fig. 2, the excited state wavepacket is expected to pass over regions of coordinate space with low singlet-triplet energy gaps, increasing the likelihood of ISC. Indeed, an ISC process occurring on a time scale that is concomitant with or faster than the time constants extracted from the temporal profiles of band (2) is supported by the results presented in Paper II[29] and the calculated spin-orbit coupling matrix element amplitudes (up to 10 meV, corresponding to maximum ISC time constants of ~ 200 fs for all ISC channels). However, as the valence electronic state density is known to be high at the $[1+2']$ and $[1+3']$ excitation levels, increasing the likelihood that SO_2^+ band (2) could be associated with IVR and singlet ionisation, band (2) alone does not allow us to definitively assign the ionisation mechanism(s) responsible for its features.

[1] A. E. Douglas, J. Chem. Phys. **45**, 1007 (1966).
[2] P. Kusch and F. W. Loomis, Phys. Rev. **55**, 850 (1939).
[3] A. E. Douglas, Can. J. Phys. **36**, 147 (1958).
[4] Y. Hamada and A. J. Merer, Can. J. Phys. **53**, 2555 (1975).
[5] R. J. Shaw, J. E. Kent, and M. F. O'Dwyer, Chem. Phys. **18**, 155 (1976).
[6] R. J. Shaw, J. E. Kent, and M. F. O'Dwyer, Chem. Phys. **18**, 165 (1976).
[7] R. Kullmer and W. Demtröder, Chem. Phys. **92**, 423 (1985).
[8] K. Kamiya and H. Matsui, Bull. Chem. Soc. Jpn. **64**, 2792 (1991).
[9] H. Müller and H. Köppel, Chem. Phys. **183**, 107 (1994).
[10] E. Hegazi, F. Al-Adel, A. Hamdan, and A. Dastageer, J. Chem. Phys. **98**, 12169 (1994).
[11] E. Hegazi, A. Hamdan, and F. Al-Adel, Chem. Phys. Lett. **221**, 33 (1994).
[12] J. Baskin, F. Al-Adel, and A. Hamdan, Chem. Phys. **200**, 181 (1995).
[13] E. Hegazi, A. Hamdan, A. Dastageer, and F. Al-Adel, Mol. Phys. **88**, 1479 (1996).
[14] A. Dastageer, E. Hegazi, A. Hamdan, and F. Al-Adel, Chem. Phys. Lett. **275**, 283 (1997).
[15] S. Bae, G. Kim, and J. Ku, Chem. Phys. Lett. **265**, 385 (1997).
[16] A. Li, B. Suo, Z. Wen, and Y. Wang, Sci. China, Ser. B: Chem. **49**, 289 (2006).
[17] H. Watanabe, S. Tsuchiya, and S. Koda, Faraday Discuss. Chem. Soc. **75**, 365 (1983).
[18] H. Watanabe, S. Tsuchiya, and S. Koda, J. Phys. Chem. **87**, 906 (1983).
[19] R. Kullmer and W. Demtröder, J. Chem. Phys. **83**, 2712 (1985).
[20] W. W. Watson and A. E. Parker, Phys. Rev. **37**, 1484 (1931).
[21] J. H. Clements, Phys. Rev. **47**, 224 (1935).
[22] R. J. Shaw, J. E. Kent, and M. F. O'Dwyer, J. Mol. Spectrosc. **82**, 1 (1980).
[23] H. Watanabe, S. Tsuchiya, and S. Koda, J. Phys. Chem. **86**, 4274 (1982).
[24] R. Kullmer and W. Demtröder, J. Chem. Phys. **81**, 2919 (1984).
[25] T. Suzuki, T. Ebata, M. Ito, and N. Mikami, Chem. Phys. Lett. **116**, 268 (1985).
[26] J. Brand, P. Chiu, A. Hoy, and H. Bist, J. Mol. Spectrosc. **60**, 43 (1976).
[27] H. Köppel, M. Döscher, and S. Mahapatra, Int. J. Quantum Chem. **80**, 942 (2000).
[28] C. Lévêque, A. Komainda, R. Taïeb, and H. Köppel, J. Chem. Phys. **138**, 044320 (2013).
[29] S. Mai, P. Marquetand, and L. González, J. Chem. Phys. **140**, 204302 (2014).
[30] A. C. Vandaele, C. Hermans, and S. Fally, J. Quant. Spectrosc. Radiat. Transfer **110**, 2115 (2009).
[31] A. Fischer, R. Kullmer, and W. Demtröder, Chem. Phys. **83**, 415 (1984).

[32]S. C. Bae, H. S. Son, G. H. Kim, and J. K. Ku, J. Phys. Chem. A **103**, 7432 (1999).

[33]H. Watanabe, S. Tsuchiya, and S. Koda, J. Chem. Phys. **82**, 5310 (1985).

[34]C. Lévêque, R. Taïeb, and H. Köppel, J. Chem. Phys. **140**, 091101 (2014).

[35]S. Becker, C. Braatz, J. Lindner, and E. Tiemann, Chem. Phys. **196**, 275 (1995).

[36]M. W. Wilson, M. Rothschild, D. F. Muller, and C. K. Rhodes, J. Chem. Phys. **77**, 1837 (1982).

[37]C. Effenhauser, P. Felder, and J. Huber, Chem. Phys. **142**, 311 (1990).

[38]K. L. Knappenberger and A. W. Castleman, J. Phys. Chem. A **108**, 9 (2004).

[39]D.-D. Zhang, Q. Ni, S.-Z. Luo, J. Zhang, H. Liu, H.-F. Xu, M.-X. Jin, and D.-J. Ding, Chin. Phys. Lett. **28**, 033301 (2011).

[40]I. V. Hertel and W. Radloff, Rep. Prog. Phys. **69**, 1897 (2006).

[41]A. Stolow and J. G. Underwood, Adv. Chem. Phys. **139**, 497 (2008).

[42]A. E. Boguslavskiy, J. Mikosch, A. Gijsbertsen, M. Spanner, S. Patchkovskii, N. Gador, M. J. J. Vrakking, and A. Stolow, Science **335**, 1336 (2012).

[43]C. Lévêque, R. Taïeb, and H. Köppel, J. Chem. Phys. **140**, 204303 (2014).

[44]T. Tsuboi, E. Y. Xu, Y. K. Bae, and K. T. Gillen, Rev. Sci. Instrum. **59**, 1357 (1988).

[45]W. C. Wiley and I. H. McLaren, Rev. Sci. Instrum. **26**, 1150 (1955).

[46]L. J. Frasinski, K. Codling, and P. A. Hatherly, Science **246**, 1029 (1989).

[47]J. Mikosch and S. Patchkovskii, J. Mod. Opt. **60**, 1426 (2013).

[48]J. Mikosch and S. Patchkovskii, J. Mod. Opt. **60**, 1439 (2013).

[49]G. Wu, A. E. Boguslavskiy, O. Schalk, M. S. Schuurman, and A. Stolow, J. Chem. Phys. **135**, 164309 (2011).

[50]J. R. Knutson, D. G. Walbridge, and L. Brand, Biochemistry **21**, 4671 (1982).

[51]M. W. Schmidt, K. K. Baldridge, J. A. Boatz, S. T. Elbert, M. S. Gordon, J. H. Jensen, S. Koseki, N. Matsunaga, K. A. Nguyen, S. Su, T. L. Windus, M. Dupuis, and J. A. Montgomery, J. Comput. Chem. **14**, 1347 (1993).

[52]T. H. Dunning, Jr., J. Chem. Phys. **90**, 1007 (1989).

[53]R. A. Kendall, T. H. Dunning, Jr., and R. J. Harrison, J. Chem. Phys. **96**, 6796 (1992).

[54]W. A. de Jong, R. J. Harrison, and D. A. Dixon, J. Chem. Phys. **114**, 48 (2001).

[55]H. Nakano, J. Chem. Phys. **99**, 7983 (1993).

[56]H. Nakano, Chem. Phys. Lett. **207**, 372 (1993).

[57]B. A. Hess, Phys. Rev. A **33**, 3742 (1986).

[58]D. G. Fedorov, S. Koseki, M. W. Schmidt, and M. S. Gordon, Int. Rev. Phys. Chem. **22**, 551 (2003).

[59]R. Englman and J. Jortner, Mol. Phys. **18**, 145 (1970).

[60]Y. Mo, J. Yang, and G. Chen, J. Chem. Phys. **120**, 1263 (2004).

[61]L. Wang, Y. T. Lee, and D. A. Shirley, J. Chem. Phys. **87**, 2489 (1987).

[62]K. Kimura, S. Katsumata, Y. Achiba, T. Yamazaki, and S. Iwata, *Handbook of He(I) Photoelectron Spectra of Fundamental Organic Molecules*, 1st ed. (Japan Scientific Societies Press, Tokyo, Japan, 1981).

[63]K. Norwood and C. Y. Ng, J. Chem. Phys. **92**, 1513 (1990).

[64]J. Erickson and C. Y. Ng, J. Chem. Phys. **75**, 1650 (1981).

[65]T. Sato, T. Kinugawa, T. Arikawa, and M. Kawasaki, Chem. Phys. **165**, 173 (1992).

[66]E. S. Wisniewski and A. W. Castleman, J. Phys. Chem. A **106**, 10843 (2002).

[67]H. Watanabe, Y. Hyodo, S. Tsuchiya, and S. Koda, Chem. Phys. Lett. **81**, 439 (1981).

[68]H. Watanabe, Y. Hyodo, S. Tsuchiya, and S. Koda, J. Phys. Chem. **86**, 685 (1982).

[69]D. L. Holtermann, E. K. C. Lee, and R. Nanes, J. Phys. Chem. **87**, 3926 (1983).

[70]R. Kullmer and W. Demtröder, J. Chem. Phys. **84**, 3672 (1986).

[71]S. C. Bae, H. S. Yoo, and J. K. Ku, J. Chem. Phys. **109**, 1251 (1998).

[72]H. S. Biswal, S. V. K. Kumar, and S. J. Wategaonkar, J. Chem. Phys. **128**, 204312 (2008).

[73]J. Brand, V. Jones, and C. di Lauro, J. Mol. Spectrosc. **40**, 616 (1971).

[74]J. C. D. Brand and R. Nanes, J. Mol. Spectrosc. **46**, 194 (1973).

[75]C.-L. Huang, S.-S. Ju, I.-C. Chen, A. J. Merer, C.-K. Ni, and A. Kung, J. Mol. Spectrosc. **203**, 151 (2000).

[76]C.-L. Huang, I.-C. Chen, A. J. Merer, C.-K. Ni, and A. H. Kung, J. Chem. Phys. **114**, 1187 (2001).

[77]F. Su, J. W. Bottenheim, D. L. Thorsell, J. G. Calvert, and E. K. Damon, Chem. Phys. Lett. **49**, 305 (1977).

[78]C. Y. R. Wu and C. Y. Ng, J. Chem. Phys. **76**, 4406 (1982).

[79]K. Norwood and C. Ng, Chem. Phys. Lett. **156**, 145 (1989).

[80]M. J. Weiss, T.-C. Hsieh, and G. G. Meisels, J. Chem. Phys. **71**, 567 (1979).

[81]G. Dujardin and S. Leach, J. Chem. Phys. **75**, 2521 (1981).

[82]K. Norwood and C. Y. Ng, J. Chem. Phys. **93**, 6440 (1990).

[83]Q. Meng and M.-B. Huang, J. Comput. Chem. **32**, 142 (2011).

[84]S. Goss, R. McLoughlin, and J. Morrison, Int. J. Mass Spectrom. Ion Process. **64**, 213 (1985).

[85]T. F. Thomas, F. Dale, and J. F. Paulson, J. Chem. Phys. **84**, 1215 (1986).

[86]L. Zhang, Z. Wang, J. Li, F. Wang, S. Liu, S. Yu, and X. Ma, J. Chen. Phys. **118**, 9185 (2003).

[87]M. H. Palmer, D. A. Shaw, and M. F. Guest, Mol. Phys. **103**, 1183 (2005).

[88]D. Golomb, K. Watanabe, and F. F. Marmo, J. Chem. Phys. **36**, 958 (1962).

[89]I. W. Watkins, J. Mol. Spectrosc. **29**, 402 (1969).

[90]M. Suto, R. L. Day, and L. C. Lee, J. Phys. B: At. Mol. Phys. **15**, 4165 (1982).

[91]B. Xue, Y. Chen, and H.-L. Dai, J. Chem. Phys. **112**, 2210 (2000).

[92]H. Kanamori, J. E. Butler, K. Kawaguchi, C. Yamada, and E. Hirota, J. Mol. Spectrosc. **113**, 262 (1985).

[93]H. Katagiri, T. Sako, A. Hishikawa, T. Yazaki, K. Onda, K. Yamanouchi, and K. Yoshino, J. Mol. Struct. **413/414**, 589 (1997).

[94]M. Brouard, R. Cireasa, A. P. Clark, T. J. Preston, C. Vallance, G. C. Groenenboom, and O. S. Vasyutinskii, J. Phys. Chem. A **108**, 7965 (2004).

[95]P. J. Singh, A. Shastri, R. D'Souza, S. B. Rao, and B. Jagatap, J. Quant. Spectrosc. Radiat. Transfer **113**, 267 (2012).

[96]W.-Z. Li and M.-B. Huang, J. Phys. Chem. A **108**, 6901 (2004).

[97]C. Xie, X. Hu, L. Zhou, D. Xie, and H. Guo, J. Chem. Phys. **139**, 014305 (2013).

[98]G. Herzberg, *Molecular Spectra and Molecular Structure Volume III - Electronic Spectra and Electronic Structure of Polyatomic Molecules*, 1st ed. (Krieger, Malabar, Florida, 1966).

[99]P. R. Bunker and P. Jensen, *Molecular Symmetry and Spectroscopy*, 2nd ed. (NRC Research Press, Ottawa, Canada, 2006).

[100]R. Speth, C. Braatz, and E. Tiemann, J. Mol. Spectrosc. **192**, 69 (1998).

[101]Y. Ralchenko, A. E. Kramida, J. Reader, and N. A. Team, NIST atomic spectra database (version 4.1) (2013).

[102]J. F. Noxon, Can. J. Phys. **39**, 1110 (1961).

[103]A. J. Merer, Discuss. Faraday Soc. **35**, 127 (1963).

[104]Y. Hamada and A. J. Merer, Can. J. Phys. **52**, 1443 (1974).

[105]K. Yamanouchi, M. Okunishi, Y. Endo, and S. Tsuchiya, J. Mol. Struct. **352/353**, 541 (1995).

[106]L. Vušković and S. Trajmar, J. Raman Spectrosc. **10**, 136 (1981).

[107]W.-Z. Li, M.-B. Huang, and B.-Z. Chen, J. Chem. Phys. **120**, 4677 (2004).

[108]Z. Yong-Feng, W. Mei-Shan, Y. Chuan-Lu, M. Mei-Zhong, P. Wei-Xiu, and M. Rong-Cai, Chin. Phys. B **17**, 4163 (2008).

[109]D. Holland, M. MacDonald, M. Hayes, P. Baltzer, L. Karlsson, M. Lundqvist, B. Wannberg, and W. von Niessen, Chem. Phys. **188**, 317 (1994).

[110]J. Eland and C. Danby, Int. J. Mass Spectrom. Ion Phys. **1**, 111 (1968).

[111]D. Lloyd and P. Roberts, Mol. Phys. **26**, 225 (1973).

[112]Z. Wang, L. Zhang, J. Li, F. Wang, and S. Yu, J. Mol. Spectrosc. **221**, 139 (2003).